

APPLIED SCIENTIFIC RESEARCH

B. ELECTROPHYSICS, ACOUSTICS, OPTICS, MATHEMATICAL METHODS

Reports published under the auspices of

*The Central National Organization for Applied Scientific
Research in the Netherlands (T.N.O.)*

*The Netherlands Physical Society,
Section for Applied Physics*

*The Royal Institute of Engineers of the Netherlands,
Section for Technical Scientific Research*

The Mathematical Centre, Amsterdam

<i>R. K. Jain</i> , On the stability of inviscid parallel flow in hydromagnetics . . .	85
<i>K. J. Nygaard</i> , A liquid scintillation coincidence counter for radiocarbon . .	89
<i>R. S. Sigmond</i> and <i>K. G. Schjetne</i> , A simple low background photon coincidence detector for tritium liquid scintillation counting	93
<i>R. Vrambout</i> and <i>L. De Greve</i> , Measurements on the magnetic anisotropy in evaporated iron films	102
<i>V. H. Weston</i> , Near-zone back-scattering from large spheres.	107
<i>R. D. Strattan</i> and <i>F. J. Young</i> , Fields in square Helmholtz coils.	117
<i>J. A. Kok</i> and <i>C. E. G. M. M. van Vroonhoven</i> , Aspects of electrical breakdown of liquid insulating material II.	125
<i>J. A. Poulis</i> , <i>C. H. Massen</i> and <i>P. van der Leeden</i> , Magnetic measurements on pure MnCO_3 , pure MnO and dissociating MnCO_3	133
<i>L. A. Peletier</i> and <i>L. van Wijngaarden</i> , Couette flow of a fully ionized gas, considered as a two-component fluid	141
<i>T. W. Edwards</i> and <i>J. van Bladel</i> , Electrostatic dipole moment of a dielectric cube	151
<i>J. Becker</i> , Skew ray tracing through toric refracting surfaces.	156
<i>L. N. Tao</i> , On theorems of minimum energy dissipation in magnetohydro- dynamics.	161

APPLIED SCIENTIFIC RESEARCH has as its objective the publication of original investigations in the realm of the applied natural sciences. It is at present issued in two sections:

- A. containing papers on applied mechanics, hydro- and aeromechanics, heat and the mechanical and thermal properties of materials;
- B. containing papers on applied electrophysics, acoustics, optics and the electrical, acoustical and optical properties of materials.

In each section one volume will comprise 480 pages and will consist of six issues of 80 pages each, published at irregular intervals. It is estimated that the publication of one complete volume will require about 1½ years. The subscription price is f 30 per volume for each section. Students may subscribe through the Secretary of the Governing and Editorial Board (address below) at the reduced price of 25 guilders.

Articles are accepted only if they deal with original research, not yet published elsewhere. They should preferably be written in English, but papers in French or German will also be accepted. Manuscripts must be typewritten, double spaced, on one side of the paper only. Illustrations should be in such form that plates can be made from them directly, the necessary ratio of reduction being if possible the same for all figures of the same article. The articles should be as concise as possible and should be preceded by a brief summary. The use of the rationalized practical system of units, which is based on the m, kg-mass and s, is recommended.

No honorarium is paid to contributors, but authors are entitled to 75 free reprints. Additional reprints may be obtained at a fixed price on prepublication order.

Governing Board:

- Prof. ir J. J. BROEZE, Delft.
- Prof. dr H. B. DORGEO, Eindhoven.
- Prof. dr H. W. JULIUS, The Hague.
- Dr G. H. REMAN, Amsterdam.
- Prof. ir J. T. THIJSSE, Delft.
- Prof. dr ir A. VAN WIJNGAARDEN, Amsterdam.

Editorial Board:

- Prof. dr R. KRONIG, Delft (General Editor).
- Prof. dr ir C. B. BIEZENZO, Delft.
- Prof. dr L. J. F. BROER, Delft.
- Dr W. DE GROOT, Eindhoven.
- Prof. dr H. A. LAUWERIER, Amsterdam.

National Editors:

- Prof. dr G. BORELIUS, Stockholm, for Sweden.
- Prof. dr A. VAN ITTERBEEK, Louvain, for Belgium.
- Prof. J. RYBNER, Copenhagen, for Denmark.
- Prof. dr M. J. O. STRUTT, Zürich, for Switzerland.
- Prof. dr S. WESTIN, Trondheim, for Norway.

Articles should be sent to the Secretary, ir H. G. DE WINTER, Laboratorium voor Technische Physica, Mijnbouwplein 11, Delft.

Overnemen van de artikelen is verboden (Art. 15, al. 3, Auteurswet 1912)

Copyright 1961. All rights reserved

PRINTED IN THE NETHERLANDS

ON THE STABILITY OF INVISCID PARALLEL FLOW IN HYDROMAGNETICS

by R. K. JAIN

Department of Mathematics, University of Delhi, Delhi, India

Summary

In the present paper we discuss the stability of parallel flow of conducting and inviscid fluid between two fixed and concentric cylinders in the presence of an axial uniform magnetic field. It will be shown that every flow $W(r)$ is stable for infinitesimal perturbations.

§ 1. *Introduction.* Recently a number of papers have appeared on the stability of rotational Couette flow in hydromagnetics by Chandrasekhar ¹⁻³), Michael ⁵), Velikhov ⁷). These authors have considered both the presence and absence of dissipative forces. But the hydromagnetic stability of parallel or nearly parallel flows has not, so far, been given much attention. However, Stuart ⁶) and Lock ⁴) have obtained the curves of neutral stability for symmetric parallel flows with different magnetic field configurations. The purpose of the present paper is to discuss similar problems in the absence of viscosity. We shall establish that every parallel flow $W(r)$ is stable, allowing only damped perturbations.

§ 2. *Formulation of the problem.* We consider the parallel flow of an inviscid and conducting fluid between two fixed and concentric cylinders of radii a and b ($b > a$). Let (r, θ, z) denote the cylindrical coordinates of a point where the common axis of the cylinders has been taken as the z -axis. Throughout the present paper cylindrical coordinates will be used. The equations of hydromagnetics are

$$\frac{\partial \mathbf{v}}{\partial t} + (\mathbf{v} \cdot \nabla) \mathbf{v} = -\frac{1}{\rho} \text{grad } p + \frac{1}{4\pi\rho} \text{curl } \mathbf{H} \times \mathbf{H}, \quad (1)$$

$$\frac{\partial \mathbf{H}}{\partial t} = \text{curl}(\mathbf{v} \times \mathbf{H}) + \frac{1}{4\pi\sigma} \nabla^2 \mathbf{H}, \quad (2)$$

$$\text{div } \mathbf{H} = 0, \quad (3)$$

$$\text{div } \mathbf{v} = 0. \quad (4)$$

It is clearly seen that these equations admit the stationary solution

$$p = \text{constant} = \Pi \text{ (say)}, \quad \mathbf{v} = [0, 0, W(r)], \quad \mathbf{H} = [0, 0, H], \quad (5)$$

where H is constant. Let the perturbed state of the system (5) be characterised by

$$p = \Pi + \tilde{\omega}, \quad \mathbf{v} = (v_r, v_\theta, v_z + W), \quad H = (h_r, h_\theta, h_z, + H), \quad (6)$$

where $\tilde{\omega}$, v_r , v_θ , v_z , h_r , h_θ and h_z are infinitesimal quantities and are chosen in the form

$$\begin{aligned} v_r &= u(r) e^{i(ct+kz)}, & h_r &= \varphi(r) e^{i(ct+kz)}, \\ v_\theta &= v(r) e^{i(ct+kz)}, & h_\theta &= \psi(r) e^{i(ct+kz)}, \\ v_z &= w(r) e^{i(ct+kz)}, & h_z &= \chi(r) e^{i(ct+kz)}, \\ \tilde{\omega} &= \tilde{\omega}(r) e^{i(ct+kz)}. \end{aligned} \quad (7)$$

Here k is a real positive number and c is a complex quantity. The first order perturbation equations are given by

$$iK\rho u = -D\tilde{\omega} + \frac{H}{4\pi} (ik\varphi - D\chi), \quad (8)$$

$$K\rho v = \frac{Hk}{4\pi} \psi, \quad (9)$$

$$i\rho K w + u\rho W' = -ik\tilde{\omega}, \quad (10)$$

$$iK\varphi = ikuH + \frac{1}{4\pi\sigma} (DD^* - k^2) \varphi, \quad (11)$$

$$iK\psi = ikvH + \frac{1}{4\pi\sigma} (DD^* - k^2) \psi, \quad (12)$$

$$ic\chi = \frac{W\varphi - uH}{r} + D(W\varphi - uH) + \frac{1}{4\pi\sigma} (D^*D - k^2) \chi, \quad (13)$$

$$D^*u + ikw = 0, \quad (14)$$

$$D^*\varphi + ik\chi = 0, \quad (15)$$

where

$$D = \frac{d}{dr}, \quad D^* = \frac{d}{dr} + \frac{1}{r},$$

$$DD^* = D^*D - \frac{1}{r^2}, \quad D^*D = \frac{d^2}{dr^2} + \frac{1}{r} \frac{d}{dr} \quad (16)$$

and

$$K = kW + c. \quad (17)$$

Equations (8)–(15) are not all independent. For instance letting (11) operate on D^* and making use of (15), we shall get (13). Elimination of v from (9) and (12) gives

$$(DD^* - k^2)\psi = \frac{i\sigma}{\rho} \left(4\pi\rho K - \frac{H^2 k^2 K^*}{|K|^2} \right) \psi. \quad (18)$$

Also elimination of $\tilde{\omega}$, w and u from (8), (10), (11), (14) and (15) gives

$$\frac{i\rho K}{\sigma} (DD^* - k^2)^2 \varphi - \left[H^2 k^2 - 4\pi\rho K^2 + \frac{i\rho k}{\sigma} \left(W'' - \frac{W'}{r} \right) \right] (DD^* - k^2) \varphi + 8\pi\rho K k W' D^* \varphi = 0. \quad (19)$$

§ 3. *Boundary conditions.* Since the boundaries are rigid, the normal component of velocity vanishes:

$$u = 0 \quad \text{at} \quad r = a, b. \quad (20)$$

We consider the boundaries to be perfectly conducting so that the Fermi boundary conditions¹⁾ are valid:

$$\phi = 0 \quad \text{at} \quad r = a, b, \quad (21)$$

$$D^* \psi = 0 \quad \text{at} \quad r = a, b. \quad (22)$$

From (11), (20) and (21) we get

$$(DD^* - k^2)\varphi = 0 \quad \text{at} \quad r = a, b. \quad (23)$$

Equation (18) is of second order, and hence two boundary conditions viz. (22), are sufficient for its solution. Equation (19) is of fourth order and for its solution four boundary conditions, viz. (21) and (23), are sufficient.

§ 4. *Proof of the theorem.* The problem has been reduced to finding the eigenvalues of c . For this purpose we consider (18) and (22)

Equation (18), on multiplication by $r\psi^*$ (ψ^* being the complex conjugate of ψ) and integration with respect to r , gives

$$\int_a^b r(|D^*\psi|^2 + k^2 |\psi|^2) dr + \frac{i\sigma}{\rho} \int_a^b r \left(4\pi\rho K - \frac{H^2 k^2 \mathbf{K}^*}{|K|^2} \right) |\psi|^2 dr = 0. \quad (24)$$

Adding the complex conjugate of (24) to it, we obtain

$$2 \int_a^b r(|D^*\psi|^2 + k^2 |\psi|^2) dr = \frac{\sigma}{\rho} c_2 \int_a^b r \left(4\pi\rho + \frac{H^2 k^2}{|K|^2} \right) |\psi|^2 dr, \quad (25)$$

where $c = c_1 + ic_2$. Equation (25) gives

$$c_2 = \frac{2\rho}{\sigma} \frac{\int_a^b r(|D^*\psi|^2 + k^2 |\psi|^2) dr}{\int_a^b r \left(4\pi\rho + \frac{H^2 k^2}{|K|^2} \right) |\psi|^2 dr} \quad (26)$$

The two integrals on the right hand side of (26) are positive, establishing thereby that $c_2 > 0$. Thus every parallel flow $W(r)$ allows only damped disturbances and consequently is stable.

Acknowledgement. I wish to thank Dr. J. N. Kapur for his guidance, encouragement and numerous discussions during the preparation of this paper. This work has been done during the tenure of a Government of India Scholarship.

Received 10th September, 1960

REFERENCES

- 1) Chandrasekhar, S., Proc. Roy. Soc. London **A 216** (1953) 293.
- 2) Chandrasekhar, S., Stability of Couette motion in hydromagnetics when the cylinders are rotating in opposite directions (to be published).
- 3) Chandrasekhar, S., Proc. Nat. Acad. Sci. **46** (1960) 253.
- 4) Lock, R. C., Proc. Roy. Soc. London **A 233** (1955) 105.
- 5) Michael, D. H., Mathematika **1** (1954) 45.
- 6) Stuart, J. T., Proc. Roy. Soc. London **A 221** (1954) 189.
- 7) Velikhove, E. P., Sov. Phys. JETP **36** no. 9 (1959) 995.

A LIQUID SCINTILLATION COINCIDENCE COUNTER FOR RADIOCARBON *)

by K. J. NYGAARD

Institutt for Teknik Fysikk, Norges Tekniske Høgskole, Trondheim, Norway

Summary

Measurements have been made of the radiocarbon counting performance of a liquid scintillation coincidence counter used in conjunction with an anticoincidence shield counter. When operated at room temperature, the system has a radiocarbon counting efficiency of 59% at a background of 16 counts/min. The activity of ethanol made from contemporary wood has been determined to 13.1 ± 0.6 disintegrations per minute per gram carbon.

§ 1. *Introduction.* The internal sample liquid scintillation counter admits the sample in the liquid (or solid) state. Thus it is usually possible to introduce larger carbon amounts into a liquid scintillation counter than into a gas counter. This is especially important in the radiocarbon dating of old samples, where a counter of high radiocarbon concentration efficiency and low background is needed. In conjunction with the Trondheim Radiocarbon Dating Laboratory an attempt was accordingly made to utilize the simple photon coincidence detector system of Sigmond and Schjetne¹⁾³⁾ for a room temperature operated radiocarbon liquid scintillation counter.

For review of liquid scintillation counters for radiocarbon dating is referred to Olsson³⁾.

§ 2. *Counting system.* The counting system is shown schematically in fig. 1. The 100 ml scintillator cell consists of a stainless steel cylinder highly polished on the inside, connected by means of teflon sealing rings to plane quartz end windows. The 13-stage venetian blind photomultiplier tubes (E.M.I. 6255) are coupled to the windows by means of thin layers of silicone oil.

*) Condensed from the author's diploma thesis, NTH 1959.

The photon coincidence detector system is almost identical with that described by Sigmond and Schjetne in their paper on tritium liquid scintillation counting, the most notable difference being that the multipliers used in the present work were somewhat more noisy. The main features of this system are that the photomultipliers are coupled directly to the coincidence circuit (the cathode followers used are not really necessary), and that the pulse height selection is performed on the coincidence circuit output pulses. This is made possible by the quasilinear coincident pulse transfer properties of the DeBenedetti-Richings coincidence circuit. For further details the reader is referred to Sigmond and Schjetne.

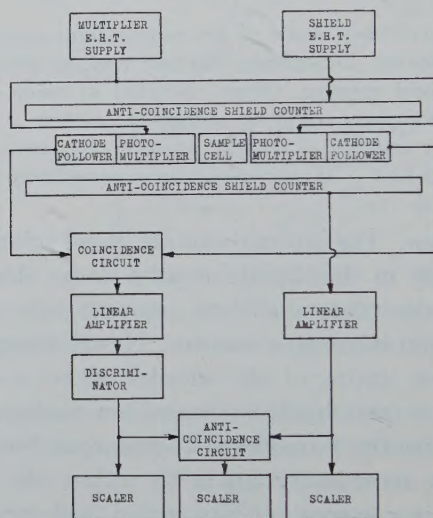


Fig. 1. Block diagram of the liquid scintillation counting system.

The scintillator cell and the photomultiplier tubes are placed inside a large anti-coincidence ring counter filled with 1 atm. propane and working in the proportional region. This is the same shielding system that is used for radiocarbon dating by Nydal⁴). The counters are surrounded by 20 cm of iron, and the laboratory itself is situated 4 m below ground level with a total of 1 m concrete above.

A scintillator solution consisting of 4 g PPO and 0.1 g POPOP per liter toluene was used throughout these experiments. The multiplier tubes were kept in darkness for some weeks prior to and during the measurements.

§ 3. *Radiocarbon counting characteristics.* Following Hayes and Ott⁵⁾, we have chosen the high voltage and the lower pulse height discriminating level of the counting system so as to maximize the value of E^2/B , E being the radiocarbon counting efficiency and B the background counting rate. No upper discriminating level was used in this work, although some additional increase in E^2/B probably could have been achieved by this means.

The curves of fig. 2 illustrate the background counting rate and the radiocarbon counting efficiency as functions of the lower discriminating level at the optimum multiplier high voltage. The curves are measured with the anti-coincidence shielding system active. The optimum lower discriminating level is indicated.

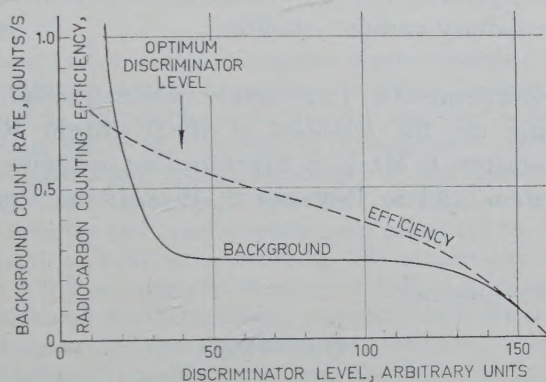


Fig. 2. Background count rate and radiocarbon counting efficiency as functions of the discriminator (lower) level at the optimum value of multiplier. E.H.T.

The performance data of the scintillation counter operated at room temperature may be summarized as follows:

- Radiocarbon counting efficiency 59%.
- Background, anti-coincidence shield passive 51 counts/min.
- Background, anti-coincidence shield active 16 counts/min.

There are experimental indications that light interaction between the multipliers and radioactive contamination in the steel cylinder are responsible for the main part of the residual background. The radiocarbon counting efficiency was determined using a benzoic acid (carboxyl C-14) standard, supplied by The Radiochemical Centre, Amersham, with a stated accuracy of 5%.

§ 4. *Activity of contemporary wood.* The counter has been used to determine the radiocarbon contents of ethanol made from contemporary wood. 7 ml of 96% ethanol was added to 93 ml of scintillator. Under the assumption that this would not change the radiocarbon counting efficiency (6), the specific activity was found, to be

13.1 ± 0.6 disintegrations/min. gram carbon.

This is in excellent agreement with recently reported values:

Hayes and Arnold ⁷⁾	13.6 ± 0.2	disint./min.	gram carbon,
Fergusson ⁸⁾	12.5 ± 0.2	„ „ „ „ „	
Nydal ⁹⁾	13.0 ± 0.1	„ „ „ „ „	

The last value pertains to the National Bureau of Standards oxalic acid "contemporary carbon" standard.

Acknowledgements. I am deeply indebted to Mr. R. Nydal for extending me the facilities of the Trondheim Radiocarbon Dating Laboratory, to Mr. R. S. Sigmond for designing the photon detector system, and to Professor S. Westin for supervision of this work.

Received 3rd November, 1960.

REFERENCES

- 1) Sigmond, R. S. and K. G. Schjetne, Appl. sci. Res. B **9** (1961) 93.
- 2) Olsson, I., Ark. Fys. **13** (1957) 37.
- 3) Sigmond, R. S. and K. G. Schjetne, NTH Technical Report T.F. 60-1.
- 4) Nydal, R., Amer. J. Sci. Radiocarbon Suppl. **2** (1960) 82.
- 5) Hayes, F. N. and D. G. Ott, LA-2095, Los Alamos Scientific Laboratory, 1957.
- 6) Hayes, F. N. and R. G. Gould, Science **117** (1953) 480.
- 7) Hayes, F. N., E. C. Anderson and J. R. Arnold, Paper P/68, Proceedings of the International Conference on the Peaceful Uses of Atomic Energy **14** (1955) 188.
- 8) Fergusson, G. J., Nucleonics **13** (1955) 23.
- 9) Nydal, R., Private communication, 1960.

A SIMPLE LOW BACKGROUND PHOTON COINCIDENCE DETECTOR FOR TRITIUM LIQUID SCINTILLATION COUNTING *)

by R. S. SIGMOND and K. G. SCHJETNE **)

Institutt for Teknisk Fysikk, Norges Tekniske Høgskole, Trondheim, Norway

Summary

The electronic system of this coincidence counter consists of two 13-stage Venetian blind photomultipliers coupled to a simple DeBenedetti-Richings coincidence circuit, followed by a medium-gain amplifier, pulse selector and scaler. The main feature of the system is its simplicity, chiefly realized by utilizing the quasi-linear transfer properties of the take-the-lesser type coincidence circuit. "Balance-point operation" permits the use of multiplier high voltage supplies and pulse amplifiers not possessing the high stability usually required for scintillation counting. The counter has been operated at 26°C with a tritium counting efficiency of 16% at a background of 100 c/min. The minimum detectable tritium concentration in water is 1.7×10^{-8} curie/liter. However, the time needed for the counter to "quiet down" after a change of sample is prohibitively long, 2-3 days. Of the background, nearly 50% seems to be caused by light interaction between the photomultipliers. Some suggestions for future improvements are given.

§ 1. *Introduction.* The main object of this investigation was the development of an efficient low background photon detector for tritium liquid scintillation counting, complying with the accessory conditions of simple electronics and room temperature operation. The instrument was chiefly intended for the investigation of natural tritium in water.

Several tritium liquid scintillation counters of fairly high efficiency and low background have been described in the literature ¹⁻¹¹). Both single photomultiplier tube spectrometers ²⁾³⁾⁴⁾ and coincidence spectrometers have successfully been used for room

*) Condensed from the N.T.H. Technical Report T.F. 60-1.

**) Now at JENER, Kjeller per Lilleström, Norway.

temperature counting of tritiated water; the best performances being efficiencies of 10–20% at backgrounds of 100–200 counts/min for water sample sizes of about 1 ml. However, in this application the single tube spectrometers require multiplier tubes specially selected for low dark current noise, while the coincidence spectrometers reported all feature a complicated and costly electronic system.

This counter employs a coincidence photon detector and thus does not require doubly selected multiplier tubes. Nevertheless its electronic system is almost as simple as that of the single tube counter. This has been achieved by using very high gain multipliers coupled through cathode followers to a coincidence circuit whose quasi-linear transfer properties permit any pulse height selection to be done after the coincidence selection. The instrument does not have the linear energy response of the commercial scintillation spectrometers and the threshold energies are accordingly more cumbersome to adjust. However, this constitutes only a minor drawback when only one specific radioisotope is to be measured.

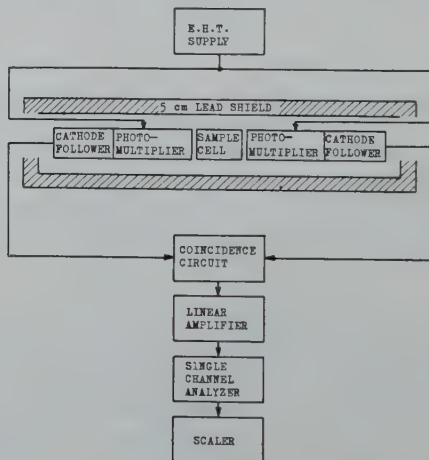


Fig. 1. Block diagram of the liquid scintillation counter.

§ 2. *Photon detector electronic system.* A block diagram of the liquid scintillation counter is given in fig. 1, while fig. 2 shows the circuit diagram of the photomultiplier-cathode follower-coincidence system together with a sketch of the scintillator cell and photomultiplier housing. The photomultipliers chosen are a matched

pair of EMI 9514A. This tube is of the Venetian blind type with 13 dynodes and a S11 CsSbO photocathode, and can be used at gains exceeding 10^8 . It has a transit time-spread of 16 nanoseconds, more than twice that of the best focused-dynode types, but this drawback is offset by a somewhat lower dark current. Moreover, the following coincidence circuit can be comparatively slow, thus making it easier to obtain some degree of linearity in the coincident pulse amplitude transfer function.

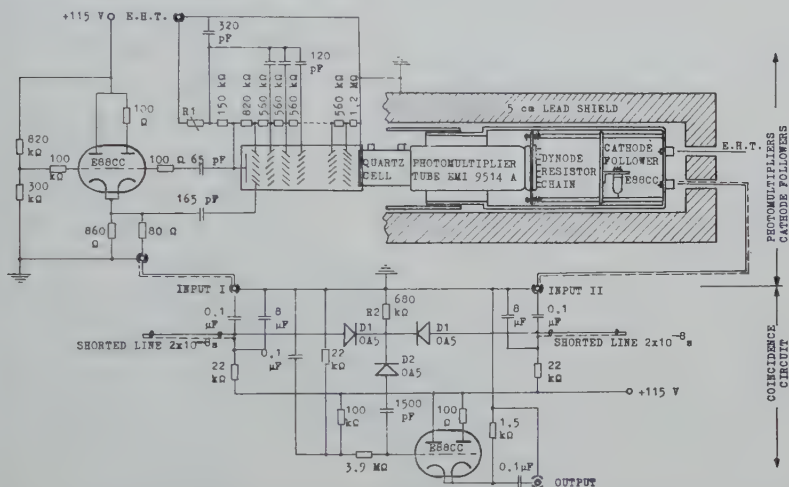


Fig. 2. Diagram of the photomultiplier - cathode follower - coincidence circuits. Sketch shows scintillator cell, photomultiplier and cathode follower housing.

The coincidence circuit is due to De Benedetti and Richings¹²⁾. It is of the take-the-lesser type, and its output pulse amplitudes thus contain a fair amount of information about the photon pulses emitted from the scintillator. The resolving time of the circuit, as defined by Bay¹³⁾¹⁴⁾, is strongly dependent on the input pulse amplitudes, increasing from 20 ns for signals of amplitudes equal to twice the lower discriminating level, to 80 ns for the maximum signal amplitudes available from the cathode followers. Most of the uncorrelated noise pulses have amplitudes below twice the lower discriminating level.

The output pulses from the coincidence circuit are quite slow, thanks to the pulse stretcher diode arrangement. Accordingly the following pulse amplifier, pulse height selector and scaler need

only have resolving times better than some tens of microseconds, as long as the expected counting rates are low. Furthermore, poor overload properties of the amplifier can be tolerated because the cathode followers preceding the coincidence circuit limit the signal amplitudes. In the present investigation the amplifier and pulse analyzer system had a resolving time of about one microsecond.

Coincident and single signal response curves for the coincidence circuit, amplifier and pulse height selector system are given in fig. 3. The tritium channel and the maximum coincidence circuit input signal amplitude are indicated. It is seen that no single signals can enter the tritium channel.

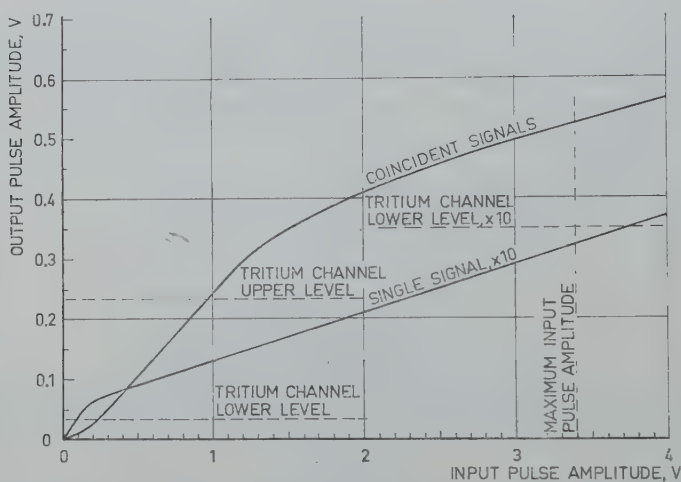


Fig. 3. Coincident and single signal response curves for the coincidence circuit, amplifier and pulse analyser system. The tritium channel and the maximum available input pulse amplitude are indicated. The single signal response curve is shown with the vertical scale enlarged $10 \times$.

At multiplier gains of 10^8 the tritium channel lower and upper levels are equivalent to 0.5 and 2.2 electrons leaving the photocathodes, respectively. Taking account of the statistical nature of the electron emission and multiplication processes and of the take-the-lesser operation of the coincidence circuit, this is just the main range of yields to be expected from tritium scintillations.

The present coincidence system has worked very well and is not critical with respect to component values. The only parameter that has to be adjusted with some care is the coincidence diode forward

bias current. An increase in this current causes an extension of the range of linear coincidence response and a decrease in the single signal rejection ratio.

§ 3. *Tritium counting* *). The work reported here was mainly concerned with the development of the photon detector electronic system. Accordingly we have chosen a scintillator and an optical system believed to be fairly efficient, without bothering much about optical optimization or ease of sample changing.

The 50 ml cylindrical quartz scintillator cell has planè end windows optically coupled to the multiplier photocathodes with thin layers of immersion oil. The cylindrical part of the wall is coated with a cellulose-base TiO_2 laquer. The scintillator solution used contains 45 ml of 50 g/l naphthalene, 7 g/l PPO and 0.05 g/l POPOP in *p*-dioxane, mixed with 5 ml water sample, and bubbled with 99,99% argon for 15 minutes in the cell ¹⁾ ¹⁵⁾. The multiplier tubes had been kept in darkness with high voltage applied for some months prior to the measurements reported below, but had to be exposed to red darkroom light for some minutes during sample changing. The cell, photomultipliers and cathode followers are placed inside a steel-lined 5 cm lead shield. The operating temperature of the scintillator and photocathodes was about 26°C during the measurements.

As the coincidence circuit has a very restricted range of linear response, the lower discriminating level as referred to the input must be considered as fixed. Thus the only important parameters that can be varied to make the tritium counting properties of the system optimum are the upper discriminating level and the multiplier high voltage.

The upper discriminating level has been set safely below the upper (overload) hump in the background pulse height spectrum (see fig. 4). The multiplier high voltage has been adjusted to maximize the tritium counting efficiency, thus making this important quantity insensitive not only to small variations in the multiplier gain, but also (because of the quasi-linear transfer properties of the coincidence circuit) to drifts in the gain of the

*) An earlier version of this counter has been used by Nygaard ¹⁷⁾ for radiocarbon measurements.

pulse amplifier. This balance-point-operation¹⁶⁾ will of course only apply to one specific isotope.

Fig. 4 shows the tritium and background pulse height spectra as seen by the pulse selector under the above conditions. Finally,

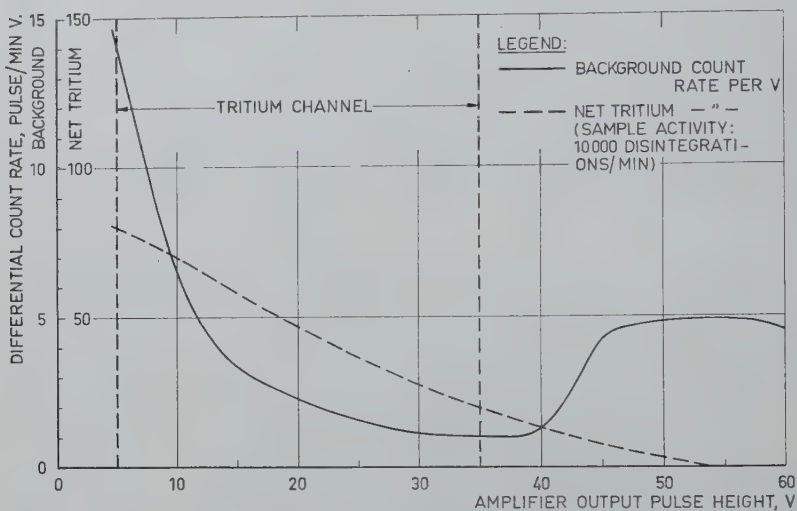


Fig. 4. Background and net tritium pulse height spectra. The tritium channel is indicated.

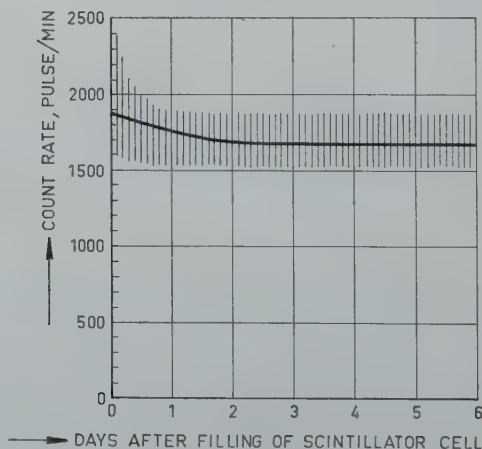


Fig. 5. Mean total count rate in tritium channel for eight 5 ml tritiated water samples, activity 10^4 disint./min, as function of time after filling of the scintillator cell. The shaded area represents the total spread of the eight count rate curves.

fig. 5 and fig. 6 show mean tritium sample and background count rates in the tritium channel for several samples as functions of time after filling of the scintillator cell. The shaded areas represent the total spread of the count rate curves. It is seen that some samples needed as much as three days to establish constant count rates. We have not investigated this effect further, but it might be due to the high operating temperature of the scintillator. However, after three days all the measurements on the 5 background and the 8 tritium samples agreed with the following counter performance data within the stated standard deviations:

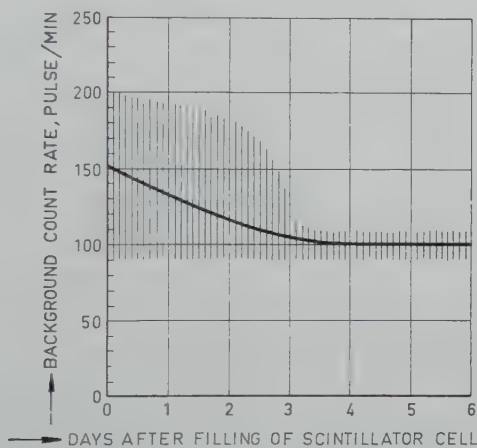


Fig. 6. Mean total count rate in tritium channel for five 5 ml distilled water samples (background) as function of time after filling of the scintillator cell. The shaded area represents the total spread of the five count rate curves.

Background count rate, tritium channel, 26°C: $100 \text{ c/min} \pm 7\%$.

Tritium counting efficiency, tritium channel: $(15.7 \pm 1.4)\%$.

The 5% uncertainty in our Harwell tritium standard has not been included in the efficiency standard deviation given above.

Following standard radiocarbon dating practice we may define the minimum quantity of tritium that can be detected as that giving a standard deviation of 25%. The sample and background counting times need not be specified in our case, the limiting factors obviously being the reproducibility of the background, and, to a lesser degree, that of the tritium counting efficiency. We find:

Minimum detectable amount of tritium: 8.6×10^{-11} Curie,

Minimum detectable tritium concentration in water: 1.7×10^{-8} Curie/liter.

Some measurements were made of the effects of the optical coupling oil and the TiO_2 diffuse reflector on the tritium counting efficiency:

Air coupling, no reflector:	7%,
Oil coupling, no reflector:	12%,
Air coupling, TiO_2 reflector:	13%,
Oil coupling, TiO_2 reflector:	15.7%.

The importance of good photon collection efficiency is evident.

A rough experimental analysis of the background gave the following approximate results:

Accidental coincidences between uncorrelated multiplier dark current noise pulses: 40 c/min (30°C), 20 c/min (26°C), 15 c/min. (24°C), 10 c/min (21°C).

Coincidences due to light interaction between the two multipliers:
> 45 c/min.

§ 4. *Conclusions.* The coincidence counter for liquid scintillation counting of tritiated water described here has some notable advantages: Room temperature operation, high concentration sensitivity and simple electronic system. Balance point operation with respect to variations in the gain of the electronic system permits the use of photomultiplier high voltage supplies and pulse amplifiers not possessing the high stability usually required for scintillation counting.

But, in the present stage of development the counter also has some serious drawbacks, the most notable apparently being associated with the scintillator. The time usually needed for the counter to "quiet down" after a change of sample is prohibitively long, 2-3 days, and even after this period the reproducibilities of the tritium counting efficiency and the background are relatively poor.

As for the future work to be done on this counter, there is a most obvious need for an investigation into the erratic behaviour of the scintillator. Furthermore, light interaction must be minimized by mounting the multipliers at right angles to each other. Stabilization of the operating temperature by means of tap-water cooling is

clearly desirable. The cathode followers preceding the coincidence circuit may be omitted.

Acknowledgements. We gratefully acknowledge the helpful discussions with Professor S. Westin and Mr. K. J. Nygaard.

Received 3rd November, 1960.

REFERENCES

- 1) Rosenthal, D. J. and H. O. Anger, *Rev. Sci. Instrum.* **25** (1954) 670.
- 2) Hodgson, T. S. and B. E. Gordon, *Liquid Scintillation Counting*, Proceedings of the Northwestern University 1957 Conference, p. 78, C. G. Bell F. N. Hayes ed. Pergamon Press 1958.
- 3) EKCO Electronics LTD, England, Leaflet L 664 A 6/59.
- 4) Nuclear Enterprises (G.B.) LTD, Scotland. Bulletin No. 20, December 1959.
- 5) Hayes, F. N. and D. G. Ott, Los Alamos Scientific Laboratory Report LA-2095 on Instruments, 1957.
- 6) Agranoff, B. W., *Liquid Scintillation Counting* see ref. 2), p. 220.
- 7) Utting, G. R., *Liquid Scintillation Counting* see ref. 2), p. 67.
- 8) Guinn, V. P., *Liquid Scintillation Counting*, see ref. 2), p. 166.
- 9) Guinn, V. P., *Proc. Symp. Advances in Tracer Applications of Tritium*, New England Nuclear Corporation, New York 1958.
- 10) Dostrovsky, I., P. Avinur and A. Nir, *Liquid Scintillation Counting*, see ref. 2), p. 283.
- 11) Audric, B. N., *Liquid Scintillation Counting*, See ref. 2), p. 288.
- 12) De Benedetti, S. and H. J. Richings, *Rev. Sci. Instrum.* **23** (1952) 37.
- 13) Bay, Z., *Nucleonics* **14** No. 4, 1956, p. 56.
- 14) *Proc. 5th Scintillation Counting Symposium I.R.E.*, *Trans Nuclear Sci.* 1956.
- 15) Furst, M., H. Kallmann and F. H. Brown, *Nucleonics* **13** (1955) 58.
- 16) Arnold, J., *Science* **119** (1954) 155.
- 17) Nygaard, K. J., *Appl. sci. Res. B* **9** (1961) 89.

MEASUREMENTS ON THE MAGNETIC ANISOTROPY IN EVAPORATED IRON FILMS

by R. VRAMBOUT and L. DE GREVE

Instituut voor Lage Temperaturen en Technische Fysica, Leuven, Belgium

Summary

We have examined the problem of the magnetic anisotropy in evaporated iron films by use of the magneto-optic Kerr effect method. As a result we found that there exists a weak anisotropy in some iron films coming from mechanical tensions.

§ 1. *Introduction.* Since a few years we have been especially interested in the magnetic structure of evaporated iron films ¹⁾²⁾. At present we report on the result of our latest measurements on magnetic anisotropy, obtained with the use of the magneto-optic Kerr effect method. This method does not only allow to study the hysteresis phenomenon of the whole film, but also at any particular point of the film. Indeed, the illuminated surface of the film can easily be reduced to a few tenths of a millimeter.

It may now safely be assumed that thin ferromagnetic films are composed of a single Weiss domain, especially after being subjected to a magnetic field. Before magnetization, Bloch walls may in some cases be found ¹⁾, but as a rule they disappear completely when an external field is applied.

We have tried to determine the different factors that influence the magnetic properties of these one-domain iron layers. When measuring as a function of thickness and especially when evaporating in a rather poor vacuum, we experienced earlier that it was practically impossible to obtain reproducible results. So we decided to restrict our investigation to layers of practically the same thickness (between 730 and 1120 Å). According to Kittel's theory ³⁾ and our own previous measurements these films should indeed be composed of only one domain.

§ 2. *Experimental method.* Our experimental method has been briefly described in an earlier paper ²⁾. In the Kerr effect a polarized lightbeam is reflected from the layer that is to be studied. This causes a small rotation of the plane of polarization. Our actual experimental device differs only little from the previously described apparatus. The CdS photoconductive cell, that was then used in order to measure the changes in light intensity after reflection, was of course not sensitive enough to measure differences in coercive fields with a sufficient accuracy. So it was replaced by a photomultiplier, in this way increasing the sensitivity of the method by several orders. This allowed us to use a weaker source of light. One of the disadvantages of a high pressure mercury arc lies in the difficulty of getting it sufficiently stabilised. So the mercury arc was replaced by a much weaker incandescent lamp of the type commonly used in microscopes.

The iron film can be rotated in its own plane between two Helmholtz coils in such a way that the magnetic field always remains parallel to the plane of the film. Hysteresis loops are then measured in different directions of the film. The angle between the long axis of the rectangular glass support and the external magnetic field varies between 0° and 180° .

The films were evaporated in a vacuum of the order of 10^{-5} to 10^{-6} mm Hg on polished rectangular glass plates. The dimensions of the layers were of the order of 3 to 4 mm in either direction. The thickness of the layers was measured by means of the optical multiple interference method of Tolansky.

§ 3. *Experimental results.* The determination of hysteresis loops as a function of the position of the layer is a very reliable method for detecting the existence of any anisotropy axis. Indeed, any change of magnetization in such films can only be attributed to a rotation of the magnetic moment in the whole film and not to the displacement of Bloch walls. Hysteresis loops which are measured parallel to an anisotropy axis should be rectangular, while loops measured perpendicular to this axis can be expected to be almost flattened out. From our measurements it appeared that often a relatively weak anisotropy occurs. Nevertheless in some layers no anisotropy can be detected. Mostly, however, the shape of the hysteresis loop and also the coercive force changes as a function

of the external magnetic field direction. Fig. 1*a* and 1*b* reproduce two hysteresis loops measured respectively parallel and perpen-

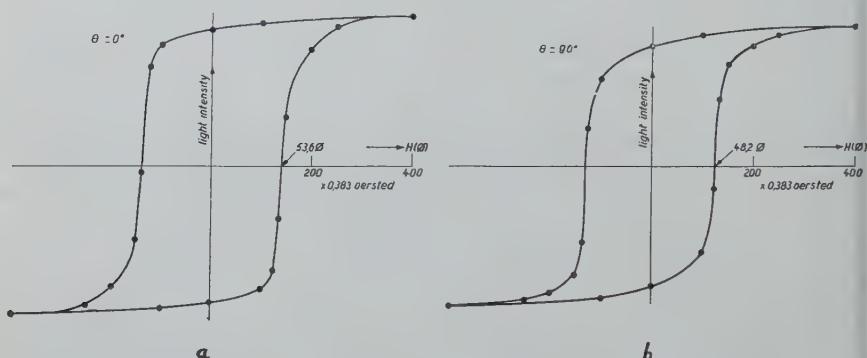


Fig. 1. Hysteresis loops measured

a) parallel b) perpendicular to the long axis of the glass support.

dicular to the long axis of the glass support for film 11. The different shapes of the curves can clearly be noticed. Fig. 2 gives the variation of coercive force as a function of the angle. There remains no

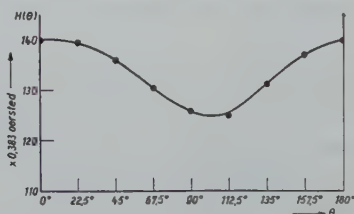


Fig. 2. Variation of coercive force as a function of the angle.

doubt that there exists a weak anisotropy axis lying closely to the long axis of the glass support.

The direction of the anisotropy axis corresponds to the direction of the maximum coercive force. As a matter of fact the anisotropy axis if existing is in all our layers either parallel to the long side of the glass support or very close to this direction. Table I contains the thickness D of the films, the angle θ between the anisotropy axis and the long axis of the support, the magnitude H_c of the coercive force measured parallel to the anisotropy axis and its maximum variation ΔH_c , i.e. the difference between the values of the coercive force measured either parallel or perpendicular to

TABLE I

No. Film	$D(\text{\AA})$	θ°	H_c (oersted)	ΔH_c (oersted)
1	860	11°	58	5
2	830	n.a.	49	—
3	890	n.a.	14	—
4	890	n.a.	25	—
5	730	0°	37.1	3.1
6	730	0°	34.4	2.4
7	730	12°	40.2	2.7
8	760	n.a.	63.2	—
9	760	0°	43.3	3.9
10	760	n.a.	42.8	—
11	745	10°	53.6	6.1
12	1120	4°	73.9	3.1

n.a.: no anisotropy could be detected.

the anisotropy axis. We must notice that the anisotropy field ΔH_c of all films is small compared to the intrinsic coercive force ($H - \Delta H_c$) of the film.

Hysteresis loops have also been measured at particular points in the layer by cutting down the illuminated area to a few tenths of a millimeter. Fig. 3a and 3b illustrate the hysteresis loops of film 11,

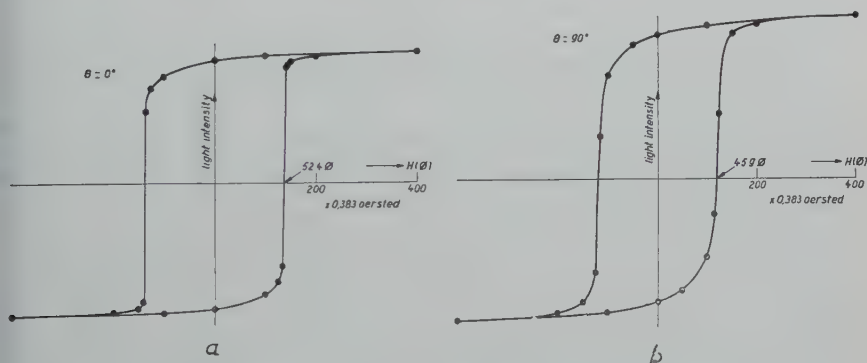


Fig. 3. Hysteresis loops for a small area of the film measured
a) parallel b) perpendicular to the long axis of the glass support.

but this time measured at a point of the film. These hysteresis loops are somewhat more rectangular than hysteresis loops of the film as a whole. The differences ΔH_c between maximum and minimum value of the coercive force slightly increases (6.9 instead of 6.1). In other films or at other points ΔH_c can also be smaller. This

means that these layers are slightly inhomogeneous, and that the values measured over the whole film can only be regarded as average values.

The influence of the shape of the film on its magnetic properties was also examined. During the same operation we evaporated circular, square and rectangular films on equal rectangular glass supports. No essential difference in their magnetical properties could be found. This seems to indicate that any anisotropy in these layers should merely be attributed to mechanical tensions, especially if no crystalline anisotropy can reasonably be expected in such complicated polycrystalline structures.

Acknowledgement. We wish to thank Prof. Van Itterbeek for putting at our disposal all the technical means of his laboratory and for his assistance. We are also grateful to the Belgian Ministry of Education and the "Union Minière du Haut-Katanga" for their financial aid.

Received 17th September, 1960

REFERENCES

- 1) Greve, L. De and J. Van Wolput, Domaines Ferromagnetiques dans des Lames de Fer Evaporées, Solid State Physics in Electronics and Telecommunications, Vol. 3, Magnetic and Optical Properties, Part I, p. 227. Edited by M. Désirant and J. L. Michels, Academic Press, London and New York.
- 2) Greve, L. De, R. Coussement and L. Sprengers, The magnetic structure of evaporated iron films. Annexe au Bulletin de l'Institut International du Froid, Copenhagen.
- 3) Kittel, C., Phys. Rev. **70** (1946) 11.

NEAR-ZONE BACK-SCATTERING FROM LARGE SPHERES *)

by V. H. WESTON

The University of Michigan, Ann Arbor, Michigan, U.S.A.

Summary

For an incident electromagnetic plane wave, the near-zone behaviour of the backscattered field produced by a perfectly conducting sphere is investigated for small wavelengths. The backscattered cross-section becomes appreciably different when the receiver approaches to within a distance of several radii from the center of the sphere, and in fact becomes the cross-section of a flat plate for the receiver very near the sphere.

§ 1. *Introduction.* An abundance of work has been done on the various problems connected with electromagnetic scattering from a sphere. Asymptotic results for small wavelengths have been given for forward, back and total cross sections. However, apart from results giving the currents on the sphere or the local behaviour of the fields in the transition region of the geometrical shadow boundary, the results hold generally only for the far field.

However, there arise many cases wherein the near field is important. One can see this in an example of a satellite orbiting the earth, or a planet at a distance of a radius from the surface. The satellite certainly is in the near zone of any signal bounced off this planet.

Here the problem that will be considered is that of the near field behaviour of the back-scattered field produced by a high frequency electromagnetic plane wave incident on a perfectly conducting sphere. It will be shown that the back-scattered cross-section differs considerably on approaching close to the scattering body.

In § 2 a modified Watson transformation will be performed on the exact Mie series answer for the back-scattered field. The behaviour

*) The research reported in this paper was supported under contract AF-30 (602)-1853 with the Rome Air Development Center.

of the portion of the scattered field due to the diffracted waves will be investigated for the near zone. In § 3 the asymptotic expression will be deduced for the portion of the back scattered field corresponding to the reflected wave for the far field. In § 4 the reflected field portion will be obtained for the near field using the Kline-Luneberg expansion.

§ 2. *Behaviour of the diffracted field contribution.* For a plane harmonic wave of the form

$$\mathbf{E}^i = \mathbf{i}_x e^{ikz - i\omega t}, \quad (1)$$

incident on an large perfectly conducting sphere of radius a , the back scattered field is given by (ref. 1), p. 564)

$$\mathbf{E}^s = -\mathbf{i}_x e^{-i\omega t} \sum_{n=1}^{\infty} (-i)^n (n + \frac{1}{2}) (a_n + ib_n), \quad (2)$$

where

$$a_n = \frac{h_n^{(1)}(kR) j_n(ka)}{h_n^{(1)}(ka)} \quad (3)$$

and

$$b_n = \frac{[kR h_n^{(1)}(kR)]' [ka j_n(ka)]'}{kR [ka h_n^{(1)}(ka)]'}. \quad (4)$$

Henceforth, the time factor $e^{-i\omega t}$ will be dropped. Using the series expansion

$$e^{-ikR} = 2 \sum_{n=0}^{\infty} (-i)^n (n + \frac{1}{2}) j_n(kR), \quad (5)$$

the following is obtained:

$$E^s(k) = (I_1 + iI_2) + \frac{i}{kR} e^{ikR - 2ika} - \frac{i}{2kR} e^{-ikR} - e^{-ikR}, \quad (6)$$

where

$$I_1 = \sum_{n=0}^{\infty} (-i)^n (n + \frac{1}{2}) [j_n(kR) - a_n(k)]. \quad (7)$$

and

$$I_2 = \sum_{n=0}^{\infty} (-i)^n (n + \frac{1}{2}) \left\{ \frac{[kR j_n(kR)]'}{kR} - b_n(k) \right\}. \quad (8)$$

The two series may be summed by contour integration giving

$$I_1 = \left(\frac{\pi}{2kR} \right)^{\frac{1}{2}} \frac{e^{i\pi}}{4} \int_C \frac{e^{\frac{1}{2}iv\pi} v}{\cos v\pi} \left[H_{v^{(2)}}(kR) - \frac{H_{v^{(1)}}(kR) H_{v^{(2)}}(ka)}{H_{v^{(1)}}(ka)} \right] dv \quad (9a)$$

and

$$I_2 = \left(\frac{\pi}{2} \right)^{\frac{1}{2}} \frac{e^{i\pi}}{4kR} \int_C \frac{e^{\frac{1}{2}iv\pi} v'}{\cos v\pi} \left\{ [\sqrt{kR} H_{v^{(2)}}(kR)]' - \frac{[\sqrt{kR} H_{v^{(1)}}(kR)]'}{[\sqrt{ka} H_{v^{(1)}}(ka)]'} [\sqrt{ka} H_{v^{(2)}}(ka)]' \right\} dv, \quad (9b)$$

where C is the contour surrounding the poles $v = \frac{1}{2}, \frac{3}{2}, \frac{5}{2}, \dots$ as shown in fig. 1.

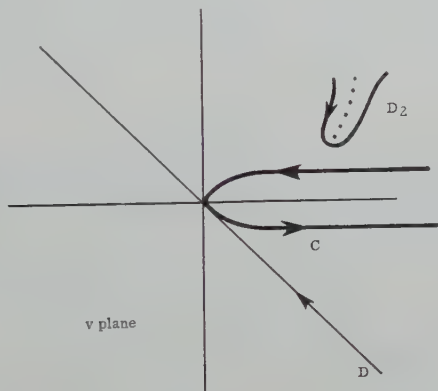


Fig. 1. Contour C in the v -plane, surrounding the poles $v = \frac{1}{2}, \frac{3}{2}, \frac{5}{2}, \dots$

It can be shown that

$$\oint_C = - \oint_{D_2} - \oint_{D_1}; \quad (10)$$

where D_2 is the contour surrounding the poles of the integrand (i.e., for I_1 the zeros of $H_{v^{(1)}}(ka)$, and for I_2 the zeros of

$$[\sqrt{ka} H_{v^{(1)}}(ka)]'$$

and D_1 is a line integral extending through the origin of the v plane. The line integral can be replaced by the integral containing the

even part with respect to v of the integrand, and this in turn can be replaced by twice the integral extending from the origin to infinity, giving

$$I_1 = \sqrt{\frac{\pi}{2kR}} e^{\frac{1}{2}i\pi} \int_0^{\infty \exp(-i\beta)} v \frac{\sin v\pi}{\cos v\pi} \cdot \frac{[H_v^{(2)}(kR) H_v^{(1)}(ka) - H_v^{(1)}(kR) H_v^{(2)}(ka)]}{2 e^{\frac{1}{2}iv\pi} H_v^{(1)}(ka)} dv \\ + \sqrt{\frac{\pi}{2kR}} e^{\frac{1}{2}i\pi} \pi \sum_{l=1,2} \frac{\bar{v}_l e^{\frac{1}{2}i\bar{v}_l\pi}}{1 + e^{i2\bar{v}_l\pi}} \frac{H_{\bar{v}_l}^{(1)}(kR) H_{\bar{v}_l}^{(2)}(ka)}{\frac{d}{d\bar{v}_l} H_{\bar{v}_l}^{(1)}(ka)} \quad (11)$$

where \bar{v}_l are the zeros of

$$H_v^{(1)}(ka) = 0, \quad \bar{v}_l = ka + (\frac{1}{6}ka)^{\frac{1}{2}} e^{\frac{1}{2}i\pi} \bar{q}_l + O\left(\frac{1}{(ka)^{\frac{1}{2}}}\right);$$

\bar{q}_l are the zeros of the Airy integral, and $0 < \beta < \frac{1}{2}\pi$.

First consider the residue portion of (11). The dominant part is the term

$$e^{i\bar{v}_l\pi} H_{\bar{v}_l}^{(1)}(kR). \quad (12)$$

Since \bar{v}_l lie above the real axis, $e^{i\bar{v}_l\pi}$ is a decaying exponential. The decaying exponent is of the order of $\bar{q}_l(ka)^{\frac{1}{2}}$. In the far field, expression (12) behaves like

$$e^{i\bar{v}_l\pi} \sqrt{\frac{2}{\pi kR}} e^{ikR - \frac{1}{2}i\bar{v}_l\pi - \frac{1}{2}i\pi},$$

and in the region where $kR \gg 1$ and $(ka)^2/R \sim O(1)$, expression (12) is

$$\sqrt{\frac{2}{\pi kR}} \exp[i\bar{v}_l\pi - \frac{1}{2}i\pi + i(kR + ka^2/2R) + i(a/R)(\frac{1}{6}ka)^{\frac{1}{2}} e^{\frac{1}{2}i\pi} \bar{q}_l],$$

and in the very near field as $R \rightarrow a$, it becomes the order of

$$e^{\frac{1}{2}i\bar{v}_l\pi}.$$

A similar analysis holds for the residues obtained by transforming the contour integral representation for the series I_2 . The residues corresponding to the diffracted field are obtained from the zeros of

$$[\sqrt{(ka)} H_v^{(1)}(ka)]',$$

which are related to the zeros of the derivative of the Airy integral.

Essentially for very large spheres, the residue terms are more important in the far field than near field in the direction of back-scattering. Physically this is what is expected. To reach a point in the near zone, the diffracted waves must creep a greater distance around the sphere, and since their attenuation depends upon distance travelled as a surface wave, the diffracted waves represented by the residue terms must be attenuated more in the near zone.

§ 2. *Behaviour of the reflected field contribution.* The integral portion of expression (11) will now be considered. This can be calculated in the same manner as is done by Scott²⁾. First it should be noted that on letting $\beta = \frac{1}{2}\pi$, the integral

$$\left(\frac{\pi}{2kR}\right)^{\frac{1}{2}} \frac{e^{\frac{1}{2}i\pi}}{2} \int_0^{-i\infty} v \frac{\sin v\pi}{\cos v\pi} e^{-\frac{1}{2}iv\pi} H_v^{(2)}(kR) dv,$$

is identically

$$\frac{1}{2} e^{-ikR}. \quad (13)$$

To obtain an asymptotic expression for the second integral in expression (11), the asymptotic expression for large ka ,

$$e^{-\frac{1}{2}iv\pi} \frac{H_v^{(1)}(kR) H_v^{(2)}(ka)}{H_v^{(1)}(ka)} = \left(\frac{2}{\pi kR}\right)^{\frac{1}{2}} \cdot \exp \left[ikR - 2ika - iv^2 \left(\frac{1}{ka} - \frac{1}{2kR} \right) + \frac{i\pi}{4} \right],$$

is substituted in the integral, giving

$$\frac{1}{2(kR)} \int_0^{\infty \exp(-i\beta)} v \tan v\pi \exp i \left[kR - 2ka - v^2 \left(\frac{1}{ka} - \frac{1}{2kR} \right) \right] dv;$$

and this, in turn, after expanding $\tan v\pi$ in a power series of $e^{-iv\pi}$, gives asymptotically

$$- \frac{a}{2(2R - a)} \exp i(kR - 2ka) \left[1 + O\left(\frac{1}{ka}\right) \right]. \quad (14)$$

The integral corresponding to I_2 may be evaluated in the same

manner to give

$$\frac{1}{2}e^{-ikR}[-i + 1/(kR)] + \frac{ia}{2(2R - a)} \left[1 + O\left(\frac{1}{ka}\right) \right] e^{ik(R-2a)}. \quad (15)$$

Hence, the reflected field portion of the back-scattered field is given by

$$-i_x e^{i(kR-2ka)} \frac{a}{(2R - a)} \left[1 + O\left(\frac{1}{ka}\right) \right]. \quad (16)$$

For more details concerning the analysis, the reader is referred to Scott's paper. However, this technique is very difficult to use in obtaining higher order terms in ka for the near field. The near field representation for the higher order terms in ka will be obtained by the method given below.

§ 3. *Near zone reflected field.* To obtain the near zone component for the reflected field portion, the Kline-Luneberg expansion will be used.

When a plane harmonic wave is incident on a perfectly conducting body, the portion of the scattered field due to reflection only can be represented in the form

$$\mathbf{E}^s = e^{iks}(\mathbf{E}_0 + \mathbf{E}_1\lambda + \mathbf{E}_2\lambda^2 + \dots). \quad (17)$$

If the incident radiation is being propagated in the direction of the z -axis and is polarized in the direction of the x -axis, and if the scattering body is a body of revolution with the z -axis as symmetry axis, then by Schensted³⁾ the above field components satisfy the relations

$$\mathbf{E}_n = \sqrt{\frac{\rho}{h_1 h_2}} \left(\mathbf{E}_n^0 + \frac{i}{4\pi} \int_f^s \sqrt{\frac{h_1 h_2}{\rho}} \nabla^2 \mathbf{E}_{n-1} ds \right) \quad (18)$$

and

$$\mathbf{E}_n^0 = \frac{i}{2\pi} (\nabla \cdot \mathbf{E}_{n-1})(-f' \hat{\rho} + \mathbf{s}), \quad n \neq 0, \quad (19)$$

where $z = f(\rho)$ defines the surface of the body, and $\rho = \sqrt{x^2 + y^2}$.

The curvilinear coordinate system (ρ, s, ϕ) is described as follows: Through each point in space (exterior to the body) there passes a ray which has been reflected from the body:

ρ is the distance from the z -axis at which the ray hits the body;

s is the sum of $f(\rho)$, and the distance along the ray from the body to the point;

ϕ is the angle between the xz -plane and the plane formed by the ray and the z -axis.

The metric coefficients are defined as follows:

$$dl^2 = h_1^2 d\rho^2 + ds^2 + h_2^2 d\phi^2;$$

and

$$h_1 = 1 + \frac{2f''(s-f)}{(f')^2 + 1}, \quad h_2 = \rho + \frac{2f'(s-f)}{(f')^2 + 1}. \quad (20)$$

In addition, Schensted³⁾ showed that

$$\mathbf{E}_0 = \sqrt{\frac{\rho}{h_1 h_2}} (-\cos \phi \hat{\mathbf{p}} + \sin \phi \hat{\mathbf{p}} \times \hat{\mathbf{p}}). \quad (21)$$

The problem, at present, is to evaluate the coefficients \mathbf{E}_n in the backscattered direction for the case when the body of revolution is the sphere.

For a sphere of radius a , the equation of the illuminated face is

$$f(\rho) = a - \sqrt{a^2 - \rho^2}, \quad (22)$$

and the back-scattered direction represented in the coordinate system (ρ, s, ϕ) is given by $\rho = 0$. If the fact is used that the back-scattered field will be polarized in the same direction as the incident field, one obtains

$$(\mathbf{E}_n \cdot \hat{\mathbf{i}}_y)_{\rho=0} = 0, \quad (\mathbf{E}_n \cdot \hat{\mathbf{i}}_z)_{\rho=0} = 0. \quad (23)$$

Thus one need only evaluate

$$(\mathbf{E}_n \cdot \hat{\mathbf{i}}_x)_{\rho=0}. \quad (24)$$

The term $\mathbf{E}_0 \cdot \hat{\mathbf{i}}_x$ can be expanded in the form

$$\mathbf{E}_0 \cdot \hat{\mathbf{i}}_x = A_0 + \rho^2(B_0 \cos 2\phi + C_0) + \rho^4(D_0 \cos 2\phi + E_0) + \dots, \quad (25)$$

and it can be shown that

$$\mathbf{E}_n \cdot \hat{\mathbf{i}}_x = A_n + \rho^2(B_n \cos 2\phi + C_n) + \rho^4(D_n \cos 2\phi + E_n) + \dots \quad (26)$$

Hence, for back-scattering

$$A_0, A_1, \dots, A_n$$

will be required, but for present purposes A_0, A_1 , and A_2 will be computed.

Now it can be shown that

$$\mathbf{E}_2^0 \cdot \mathbf{i}_x \sim O(\rho^2), \quad (27)$$

and

$$\mathbf{E}_1^0 \cdot \mathbf{i}_x \sim O(\rho^4). \quad (28)$$

Thus, one obtains

$$\mathbf{E}_2 \cdot \mathbf{i}_x = \frac{i}{4\pi} \sqrt{\frac{h_1 h_2}{\rho}} \int_0^s \sqrt{\frac{h_1 h_2}{\rho}} \nabla^2(\mathbf{E}_1 \cdot \mathbf{i}_x) ds + O(\rho^2), \quad (29)$$

and

$$\mathbf{E}_1 \cdot \mathbf{i}_x = \frac{i}{4\pi} \sqrt{\frac{h_1 h_2}{\rho}} \int_t^s \sqrt{\frac{h_1 h_2}{\rho}} \nabla^2(\mathbf{E}_0 \cdot \mathbf{i}_x) ds + O(\rho^4). \quad (30)$$

In order to compute $(\mathbf{E}_2 \cdot \mathbf{i}_x)_{\rho=0}$, the term $[\nabla^2(\mathbf{E}_1 \cdot \mathbf{i}_x)]_{\rho=0}$ is required.

It can be shown that if

$$u = (A_n + \rho^2 C_n + \rho^4 E_n + \dots) + \cos 2\phi(B_n \rho^2 + D_n \rho^4 + \dots), \quad (31)$$

where A_n, C_n, B_n, \dots are functions of s only; then

$$\nabla^2 u = (A_n^* + \rho^2 C_n^* + \rho^4 E_n^* + \dots) + \cos 2\phi(B_n^* \rho^2 + D_n^* \rho^4 + \dots), \quad (32)$$

where

$$A_n^* = \frac{\partial^2 A_n}{\partial s^2} + \left(\frac{4}{2s + a} \right) \frac{\partial A_n}{\partial s} + 4C_n \left(\frac{a}{2s + a} \right)^2, \quad (33)$$

and C_n^* depends upon A_n, C_n, E_n only. All the starred coefficients are functions of s only.

Thus in order to compute $[\nabla^2(\mathbf{E}_1 \cdot \mathbf{i}_x)]_{\rho=0}$, only the coefficients A_1 and C_1 are required and, similarly, in order to compute A_1 and C_1 the quantities A_0, C_0 , and E_0 are required. These in turn are found from the expression

$$\begin{aligned} \mathbf{E}_0 \cdot \mathbf{i}_x &= \sqrt{\frac{\rho}{h_1 h_2}} (-\cos \phi \hat{\rho} + \sin \phi \hat{\phi}) \cdot \mathbf{i}_x \\ &= -\frac{1}{(f')^2 + 1} \sqrt{\frac{\rho}{h_1 h_2}} + \cos 2\phi \frac{(f')^2}{(f')^2 + 1} \sqrt{\frac{\rho}{h_1 h_2}} \\ &= (A_0 + C_0 \rho^2 + E_0 \rho^4 + \dots) + \cos 2\phi (B_0 \rho^2 + \dots). \end{aligned} \quad (34)$$

Computing the coefficients, the following is obtained:

$$[\mathbf{E}_0 \cdot \mathbf{i}_x]_{\rho=0} = -\frac{a}{(2s+a)}, \quad (35)$$

$$[\mathbf{E}_1 \cdot \mathbf{i}_x]_{\rho=0} = \frac{i}{4\pi} \left[\frac{1}{(2s+a)} - \frac{2a}{(2s+a)^2} + \frac{a^2}{(2s+a)^3} \right], \quad (36)$$

$$[\mathbf{E}_2 \cdot \mathbf{i}_x]_{\rho=0} = \frac{-1}{16\pi^2} \left[\frac{1}{(2s+a)^2} - \frac{3a}{(2s+a)^3} + \frac{5a^2}{(2s+a)^4} - \frac{3a^3}{(2s+a)^5} \right]. \quad (37)$$

Now for back-scattering, s is given by the relation $s = R - a$, where R is the distance of the observation point from the center of the sphere. Hence, the reflected field is given by

$$\mathbf{E}_s = -\mathbf{i}_x \frac{a}{(2R-a)} e^{ik(R-2a)} \left[1 + \frac{a_1}{ka} + \frac{a_2}{(ka)^2} + \frac{a_3}{(ka)^3} + \dots \right], \quad (38)$$

where

$$a_1 = -\frac{i2(R-a)^2}{(2R-a)^2}, \quad (39)$$

and

$$a_2 = \frac{a(R-a)(2R^2 - 4Ra + 3a^2)}{(2R-a)^4}. \quad (40)$$

§ 4. *Comments.* The back-scattered cross-section is defined by

$$\sigma = \lim_{r \rightarrow \infty} 4\pi r^2 |\mathbf{E}^s|^2 / |\mathbf{E}^i|^2. \quad (41)$$

However, this is usually defined for the far-field where the distance r is the distance from the scattering object to the receiver. However, in the near zone the distance r is ambiguous since the body no longer looks like a point source. For near-zone back-scattering from the sphere, it is best to take r as the distance from the specular point to the receiver. Hence, if R is the distance from the centre of the sphere of radius a , r is given by $r = R - a$. In the far field r asymptotically approaches R ; hence, in the cross-section expression, r may be replaced by R .

For the near field the back-scattered cross-section may be obtained using (38), giving

$$\sigma = \pi a^2 \left(1 + \frac{a}{2r}\right)^{-2} \left[1 + O\left(\frac{1}{(ka)^2}\right)\right]. \quad (42)$$

Hence, it is seen that the cross-section decreases as the receiver approaches the sphere. These results hold, provided that the wavelength is sufficiently large, such that the diffracted field is negligible in the far zone. It was shown in § 1 that the contribution of the diffracted field to back-scattering is even less in the near field.

Note added in proof:

It is interesting to note that

$$\sigma = 4\pi r^2, \quad r \ll a,$$

$$\sigma = \frac{4}{9}\pi a^2, \quad r = a,$$

$$\sigma = \pi a^2, \quad r \gg a.$$

For the first case, the backscattered cross-section is that of a flat plate which is expected, and the third case is the usual far field radar cross-section of a sphere.

Received 21st August, 1960

REFERENCES

- 1) Stratton, J. A., *Electromagnetic Theory*, McGraw-Hill, New York, 1941.
- 2) Scott, J. M. C., *An Asymptotic Series for the Radar Scattering Cross Section of a Spherical Target*, A.E.R.E., Report T/M, 30, 1949.
- 3) Schensted, C., *J. Appl. Physics* **26** (1955) 306.

FIELDS IN SQUARE HELMHOLTZ COILS

by R. D. STRATTAN and F. J. YOUNG

Carnegie Institute of Technology, Pittsburgh, Pennsylvania, U.S.A.

Summary

The axial component of the magnetic field in square Helmholtz coils of rectangular cross-section is investigated. Expressions for the axial field are derived and simplified enough so that any specific case can be easily calculated with a small internally programmed digital computer. Plots of the field at the centre of the coils as a function of winding thickness with coil spacing as a parameter are presented. Curves of the variation of the field with distance from the centre are given. Spherical volumes in which the axial magnetic field varies 1% and 2% are computed for various configurations. The dimensions of the coils which hold the field variations to 1% and 2% over the maximum spherical volume are given.

§ 1. *Introduction.* The square Helmholtz pair shown in fig. 2 can be used to produce uniform magnetic fields in the vicinity of

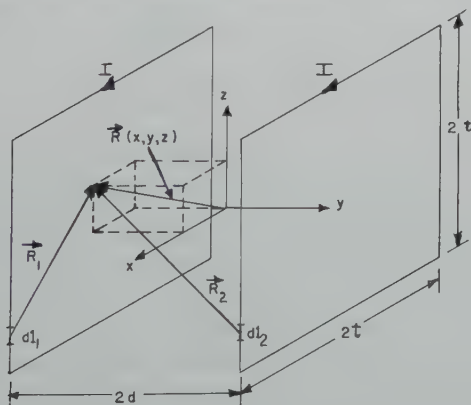


Fig. 1. Square current filaments.

the origin of the coordinates. In applications such as the rictometer where more than one Helmholtz pair is needed square Helmholtz

coils are more compact and consume less power than ordinary Helmholtz pairs. In the case of $\beta = 0.80$ and $\alpha = 0.15$ for the inside pair of a two phase-arrangement consisting of two Helmholtz pairs a circular set of coils require about 43% more copper to produce the same magnetic field at the same current density than a set comprising square coils. The copper losses are correspondingly greater for circular than square coils in arrangements where more than two Helmholtz pairs are required.

§ 2. *Calculation of the magnetic field.* The field due to a coil system similar to the one shown in fig. 2 can be found at any point

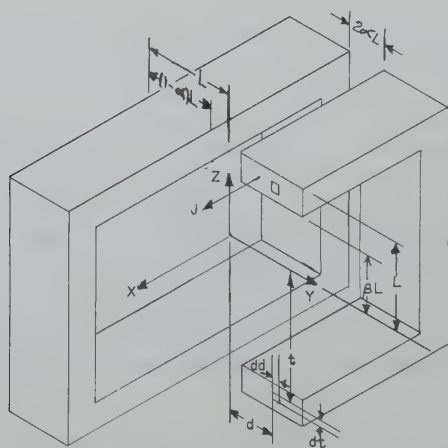


Fig. 2. Square coils filling a cubical.

in space from Ampere's law and integration over the winding cross-section. The final integral cannot be performed analytically but is easily evaluated with the aid of a digital computer and Simpson's rule. The only case calculated here is for the overall axial dimension equal to the transverse dimensions. However this method is applicable to any rectangular prism shape.

The parameters of this coil system are α , the dimensionless spacing between the coil sections, and β , the dimensionless measure of the winding thickness. The gap of $2\alpha L$ is placed between the coil sections to give a more uniform field and to provide better access to the interior of the coils.

Only the axial field component is calculated, although the radial

components can be calculated by the same method. First the axial field component due to the two current filaments shown in fig. 1 is found from Ampere's law. Then using this as the field due to the infinitesimal winding areas dd by dt , the total field is found by integrating over d from αL to L and over t from βL to L . Rationalized MKS units are used in this paper.

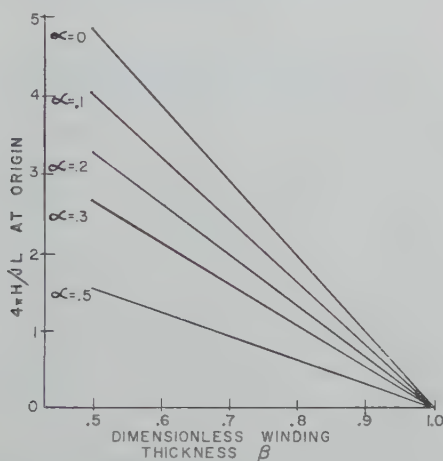


Fig. 3. The magnetic field at the origin as a function of coil spacing and winding thickness.

The field $d\mathbf{H}$ at (x, y, z) due to the current elements $d\mathbf{l}_1$ and $d\mathbf{l}_2$ in fig. 1 is given by

$$d\mathbf{H} = I(d\mathbf{l}_1 \times \mathbf{a}_{r_1})/4\pi r_1^2 + I(d\mathbf{l}_2 \times \mathbf{a}_{r_2})/4\pi r_2^2,$$

$$\frac{\mathbf{a}_{r_1}}{r_1^2} = \frac{\mathbf{a}_x(x - x_1) + \mathbf{a}_y(y + d) + \mathbf{a}_z(z - z_1)}{[(x - x_1)^2 + (y + d)^2 + (z - z_1)^2]^{\frac{3}{2}}},$$

$$\frac{\mathbf{a}_{r_2}}{r_2^2} = \frac{\mathbf{a}_x(x - x_2) + \mathbf{a}_y(y - d) + \mathbf{a}_z(z - z_2)}{[(x - x_2)^2 + (y - d)^2 + (z - z_2)^2]^{\frac{3}{2}}}.$$

x_1, x_2, z_1 and $z_2 = \pm t$ in order to define the current filament. Taking only the y component of the field,

$$\frac{4\pi H}{I} = \int_{-t}^t \left\{ \frac{(x + t) dz_1}{[(x + t)^2 + (y + d)^2 + (z - z_1)^2]^{\frac{3}{2}}} \right. \\ \left. + \frac{(x + t) dz_2}{[(x + t)^2 + (y - d)^2 + (z - z_2)^2]^{\frac{3}{2}}} \right\}$$

$$\begin{aligned}
& + \frac{(t-x) dz_1}{[(x-t)^2 + (y+d)^2 + (z-z_1)^2]^{\frac{3}{2}}} \\
& + \frac{(t-x) dz_2}{[(x-t)^2 + (y-d)^2 + (z-z_2)^2]^{\frac{3}{2}}} \\
& + \frac{(z+t) dx_1}{[(x-x_1)^2 + (y+d)^2 + (z+t)^2]^{\frac{3}{2}}} \\
& + \frac{(z+t) dx_2}{[(x-x_2)^2 + (y-d)^2 + (z+t)^2]^{\frac{3}{2}}} \\
& + \frac{(t-z) dx_1}{[(x-x_1)^2 + (y+d)^2 + (z-t)^2]^{\frac{3}{2}}} \\
& + \frac{(t-z) dx_2}{[(x-x_2)^2 + (y-d)^2 + (z-t)^2]^{\frac{3}{2}}} \Bigg\}.
\end{aligned}$$

This integral can be evaluated using the following identity:

$$\int_{-t}^t \frac{dx}{[(a-x)^2 + b^2 + c^2]^{\frac{3}{2}}} = \frac{1}{(b^2 + c^2)} \left\{ \frac{(t+a)}{[(a+t)^2 + b^2 + c^2]^{\frac{3}{2}}} + \frac{(t-a)}{[(a-t)^2 + b^2 + c^2]^{\frac{3}{2}}} \right\}.$$

If we define a quantity $C_{i,j,k}(x/t, y/t, z/t, d/t)$ as follows;

$$\begin{aligned}
C_{i,j,k} = & \left\{ \frac{1}{[1 + (-1)^i x/t]^2 + [d/t + (-1)^j y/t]^2} \right. \\
& \left. + \frac{1}{[1 + (-1)^k z/t]^2 + [d/t + (-1)^j y/t]^2} \right\} \\
& \cdot \frac{[1 + (-1)^i x/t][1 + (-1)^k z/t]}{[(1 + (-1)^i x/t)^2 + (d/t + (-1)^j y/t)^2 + (1 + (-1)^k z/t)^2]^{\frac{3}{2}}},
\end{aligned}$$

then the field due to the current filaments of fig. 1 is

$$\frac{4\pi H}{I} = \sum_{i=1}^2 \sum_{j=1}^2 \sum_{k=1}^2 (1/t) C_{i,j,k}(x/t, y/t, z/t, d/t).$$

The field due to the coil configuration shown in fig. 2 is then

$$\frac{4\pi H}{JL} = \sum_{i=1}^2 \sum_{j=1}^2 \sum_{k=1}^2 \int_{\beta}^1 d(t/L) \int_{\alpha L/t}^{L/t} d(d/t) C_{i,j,k}(x/t, y/t, z/t, d/t).$$

With the substitutions

$$[(1 + (-1)^i x/t)^2 + (1 + (-1)^k z/t)^2]^{\frac{1}{2}} \tan u = d/t + (-1)^j y/t$$

and $\sin u = w$ the integration over d/t reduces to the form

$$\int \frac{dw}{p^2 + w^2} = (1/p) \arctan (w/p).$$

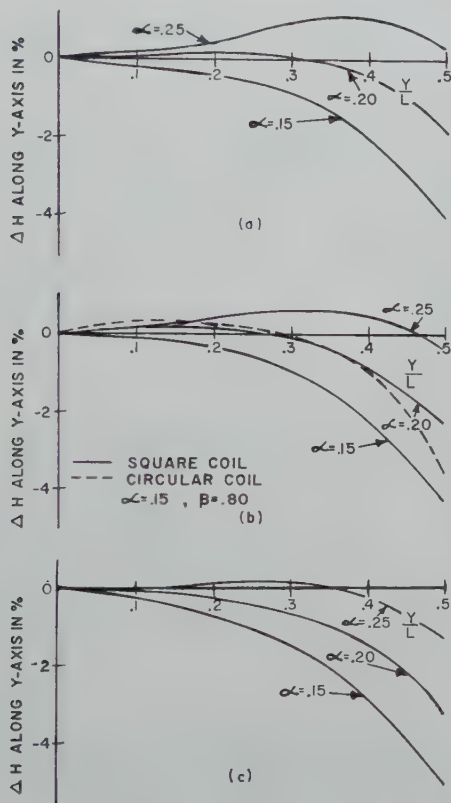


Fig. 4. Variation of axial field uniformity along the y -axis;
(a) $\beta = 0.75$, (b) $\beta = 0.80$, (c) $\beta = 0.85$.

The result is

$$\int_{\alpha L/t}^{L/t} C_{i,j,k} d(d/t) = \sum_{m=1}^2 \sum_{n=1}^2 (-1)^m \arctan \phi_{i,j,k}^{m,n}(x/L, y/L, z/L, t/L)$$

where for $m = 1$ and $n = 1$ $\phi_{i,j,k}^{m,n}$ is defined as

$$\frac{[t/L + (-1)^k z/L][\alpha + (-1)^j y/L]}{[t/L + (-1)^i x/L][t/L + (-1)^i x/L)^2 + (t/L + (-1)^k z/L)^2 + (\alpha + (-1)^j y/L)^2]^{\frac{1}{2}}}.$$

For $m = 2$, the expression is the same except that α is replaced by one; and for $n = 2$, $(-1)^i x/L$ and $(-1)^k z/L$ are interchanged. The total field in the axial direction then becomes

$$\frac{4\pi H}{JL} = \sum_{i=1}^2 \sum_{j=1}^2 \sum_{k=1}^2 \sum_{m=1}^2 \sum_{n=1}^2 (-1)^m \int_{\beta}^1 \arctan \phi_{i,j,k}^{m,n}(x/L, y/L, z/L, t/L) d(t/L).$$

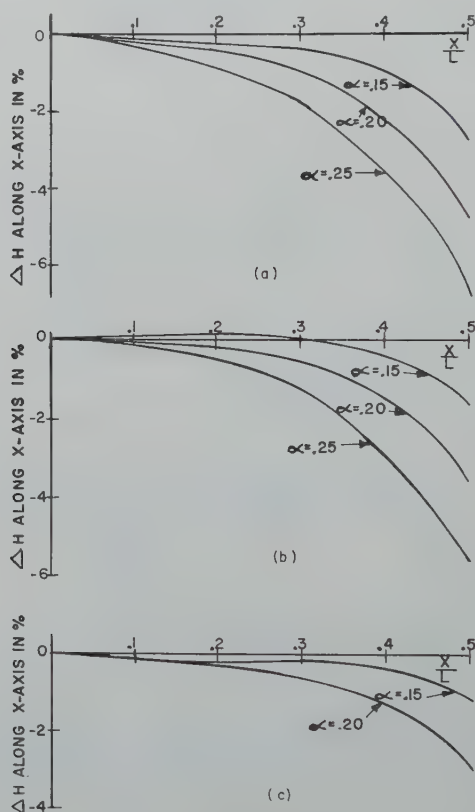


Fig. 5. Variation of axial field uniformity along the x -axis;
(a) $\beta = 0.75$, (b) $\beta = 0.80$, (c) $\beta = 0.85$.

This integral was evaluated numerically on the C.I.T. IBM 650 digital computer using arctangent and Simpson's rule subroutines.

§ 3. *Results and conclusions.* The field at the centre of the coil system as a function of α and β is shown in fig. 3. For the ranges of α and β shown the field at the centre is given very nearly by

$$H = 0.716 (1 - \alpha)(1 - \beta) JL \text{ amp-turns/meter.}$$

The percent deviation of the field from its value at the origin is given at points along the y and x axes by figs. 4 and 5 respectively for several values of dimensionless winding thickness.

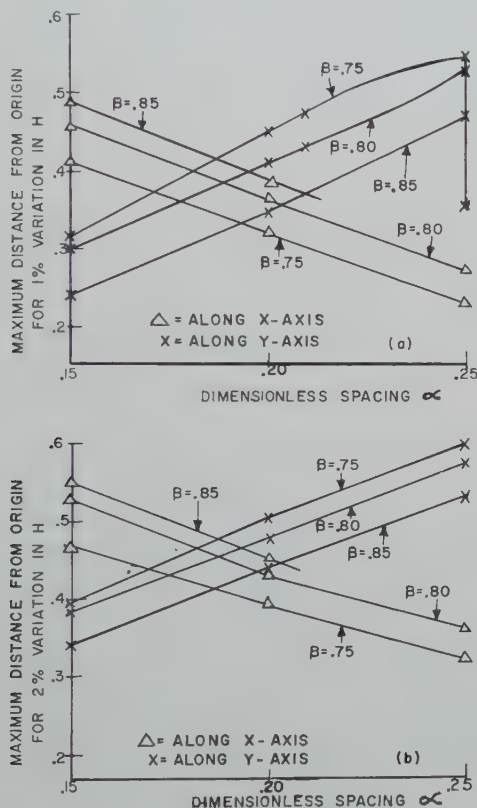


Fig. 6. The maximum distance from the origin for (a) 1%; or (b) 2% field variation. Intersection of equal β curves yield values of α and β for spherical region of uniformity. Maximum spherical volumes occur for $\alpha = 0.185$, $\beta = 0.80$ with radius = $0.38 L$ at 1% uniformity and $0.45 L$ at 2% uniformity.

The maximum distance from the origin for 1% and 2% variation in the axial field as a function of α for a given β is shown in fig. 6.

The abscissae of the intersections of equal β curves are the α 's for maximum radius of a spherical volume of 1% or 2% uniformity. The maximum spherical volume occurs for $\beta = 0.80$, $\alpha = 0.185$ with a radius for 1% variation of $0.38 L$.

The percentage variation of the axial field of a solenoid of length $2R$, outer radius R , inner radius $0.80 R$ with the windings omitted for $0.15 R$ on either side of the midplane is shown in fig. 4(b) for comparison. The field at the centre of the solenoid is $H = 0.115JR$ amp-turns/meter, while that of the cubical coil is $H = 0.122JL$ amp-turns/meter for $\alpha = 0.15$, $\beta = 0.80$.

Received 17th October, 1960.

ASPECTS OF ELECTRICAL BREAKDOWN OF LIQUID INSULATING MATERIAL II

by J. A. KOK and C. E. G. M. M. VAN VROONHOVEN

Philips Research Laboratories N.V. Philips' Gloeilampenfabrieken,
Eindhoven-Netherlands

Summary

Part I of this investigation is continued by considerations on the adsorption of soaps and resins to the impurities which float in the insulating liquid. It was shown that soaps may stabilize the suspension, and resins may do likewise, but if applied both in a certain proportion immediate flocculation and lowering of the breakdown-strength may follow. The action of colloid chemical stabilizers or inhibitors originating from research on dyes has been tentatively explained.

§ 1. § 1. *Introduction.* In part I (ref. 1)) a discussion was given of the relation between the breakdown-strength of liquid insulators and the diameter of the insoluble impurities. If the radii r of the particles are equal and if their dielectric constant is infinite, then the polarizability may be assumed to be proportional to r^3 . If there happens to be a local stress concentration of thrice the average field strength, such as occurs on top of a hemispherical hump on one of the electrodes, then the breakdown strength E_0 , occurring after a long duration of time, may be shown to depend only on r , the absolute temperature T , Boltzmann's constant k and the permittivity of the dielectric ϵ_0 :

$$\epsilon_0 r^3 E_0^2 = \frac{1}{4} k T. \quad (1)$$

With $T = 300^\circ\text{K}$ and $\epsilon_0 = 1$ this formula gives for $E_0 = 25 \text{ kV/mm}$: $r = 25 \text{ \AA}$; $E_0 = 100 \text{ kV/mm}$: $r = 9.5 \text{ \AA}$. The relation was shown to be valid for suspensions of particles having a diameter of about 1 micron (10000 \AA).

The size of the particles in aqueous suspension may be treated by means of considerations based on calculations carried out by

Overbeek, Verwey and Hamaker ²⁾. By the attractive London-van der Waals forces the particles tend to unite. In an ionogenic medium such as water the particles will gather a repulsive ion atmosphere. Their repulsion is proportional to the particle radius, whereas the attraction by Van der Waals forces does not keep up with it. In aqueous media a suspension will thus be stabilized after the particles have obtained a radius of 500 to 3000 Å.

In pure hydrocarbon oil the stabilizing ion atmospheres of the particles are very diluted and may be stripped off by the electrophoretic motion by collisions against ions. However, stabilization of a suspension in hydrocarbon oil may nevertheless take place if surface-active substances such as soaps are present in the oil. A well-known application of soaps in aqueous suspensions consists in keeping soil particles dispersed in the process of laundering, thereby preventing flocculation of the particles and graying of the laundry.

Constructive criticism of the views expressed in the first article (I) was brought forward by H. Koelmans, who pointed at the difference in the mechanisms of stabilization in aqueous suspension and suspensions in several hydrocarbon oils.

§ 2. *Colloid particles in oil, stabilized by soluble soaps or oxidation resins.* Soaps in mineral oil are considered to lower its insulating value. It will be shown here that addition of a small amount of soaps may improve the breakdown strength of the oil by stabilization of the colloid impurities it contains. However, if oxidation resins are present in the oil, an increasing soap content may be the cause of flocculation and a decreasing breakdown strength.

A simple fatty acid may be represented by RCOOH , in which R is an aliphatic chain. The corresponding soaps formed may be RCOO Na or $(\text{RCOO})_2 \text{Ca}$. The heavier soap molecules with 14 to 22 carbon atoms may have a length of 20 to 35 Å. Micellar structures around impurities in oil containing soap molecules, which tend to be adsorbed to the impurities, may easily obtain a diameter of 50 to 100 Å, which is the size we need for our theory of electrical breakdown. Physical adsorption (by mirror image forces or Van der Waals forces, etc.) or chemisorption may play a part in this surface activity. If the energy of adsorption is very large, chemisorption plays a part, whereas physical adsorption liberates a lesser amount of energy (see ref. ³⁾).

As interfaces are the seat of electrical charges or electrical double sheaths, polarizable molecules or charged ions and particles may become adsorbed at the interface of different phases (see fig. 1). Fig. 2 shows several examples of soap molecules adsorbed to water droplets in oil, oil droplets in water etc. Sometimes a double cover of soap molecules occurs at a water droplet in oil. If such a double cover of soap molecules comes into existence, the diameter of the

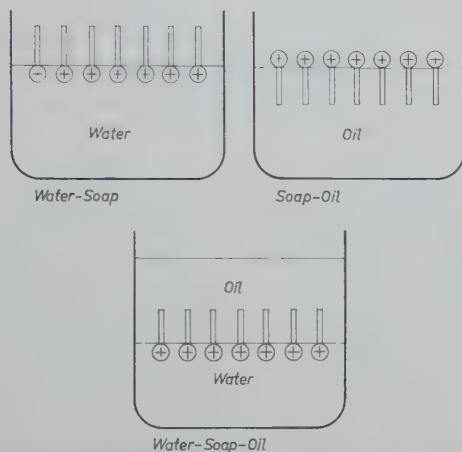


Fig. 1. The interface of two phases (oil, air and water) is an electrical double sheath at which charged or polarizable molecules or ions (in this case soaps) gather. See W. W. Niven, *Fundamentals of detergency*, 1950.

Reinhold Publ. Co., N. York.

particles increases. If the soap molecules have a length of say 25 \AA , then the particle diameters may increase from 50 \AA to 100 \AA , giving a lowering of the breakdown strength from 25 kV/mm to 9 kV/mm . Thus the formation of soaps in the long run will be harmful to the insulating oil, even if no resins are present. It all depends on the interface energies between the three or two substances (see ref. ³).

Van der Minne, Hermanie, Van der Waarden, Mackor and Van der Waals jr.⁴) studied the stabilization of carbon black particles by adsorption of soaps or oxidation resins in mineral oil. Van der Waarden assumed a mechanism of attraction different from the London-Van der Waals forces. He assumed the surface area of the carbon black particles to be densely occupied by polar carbon-oxygen bonds, which supposition was proved by an analysis of the mixture of the adsorbed gases. The product contained 9.2

per cent of the unavoidable water and 6 per cent (by weight) of oxygen, of which one half could not be removed by heating at 200°C and was assumed to be chemically bound.

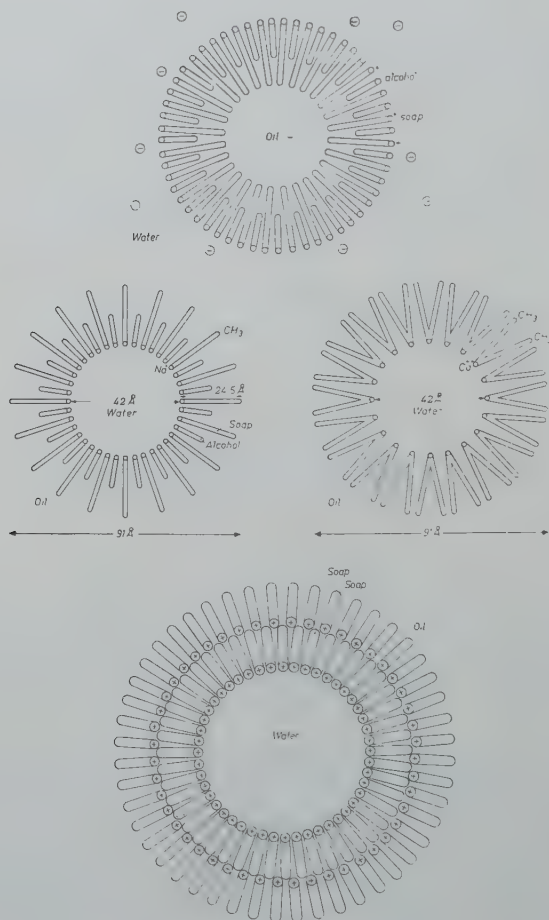


Fig. 2. Different types of micelles formed around an oil droplet in water or a water droplet in oil.

Those dipoles formed by carbon and oxygen attract polar or highly polarizable molecules. In the case of a soap molecule the inorganic head of the molecule will be preferentially adsorbed to the carbon particle (or the water droplet), whereas their organic tails may be sticking out tens of Å's (see fig. 2).

Aromatic parts of molecules show a far greater interaction with polar molecules or particles than aliphatic molecules, which may be ascribed to the pronounced polarizability of aromatic nuclei in the plane of the rings (Kerr-effect). Thus aromatic parts of molecules or metal ends of soap molecules will be strongly adsorbed by carbon particles or to water droplets, their aliphatic side chains protruding like tentacles from the carbon or water surface. If they are sticking out like thorns, the surfaces of carbon particles are being kept apart by steric hindrance at a distance of $2l$ (l is the length of a side chain) and flocculation will hardly be possible if $2l$ exceeds a value of 40 \AA , which is about the diameter of the Van der Waals sphere of attraction.

Adsorption of rods of 20 \AA length was shown to stabilize a suspension of carbon particles of about 5000 \AA diameter, whereas with rods of 10 \AA rapid flocculation occurred (see ref. 4) and 5)).

The action of aromatic colloid-chemical stabilizers or inhibitors in insulating oils may consist in a prevention of flocculation of impurities by supplying the impurities with a protective cover against further flocculation. It is no wonder that paint and dye research has supplied many inhibitors for the construction of cables, transformers and capacitors. Both strive to supply a protective cover to fibre-like solid hydrocarbons, see § 4.

§ 3. *Electrolyte contents of insulating oil and flocculation of particles.* Electrolytes may be present in insulating oil and are responsible for a certain electrical conductivity different from zero. The work of several investigators, as cited by Van der Minne, Van der Waarden 4) and Koelmans 5) had made it clear that ions are present in liquid hydrocarbons. It is not clear to the author whether these ions always consist of ionized oil molecules or whether they should be attributed to the presence of foreign matter.

A number of investigators 4) 5) have shown that a soap molecule of calcium di-isopropyl salicylate (abbreviated to Ca-"dips") in oil, if adsorbed to a carbon particle, may be dissociated, imparting a positive charge to the particle, whereas tetra-isoamyl ammonium picrate ("tiap") gives it a negative electric charge. This corresponds to the ions adsorbed and the counter ion atmospheres of the particles in aqueous suspensions, which may produce attractive or repulsive forces. As the carbon-soap and carbon-oxidation resin micelles have

opposite charges, flocculation may occur at every collision of these micelles.

Thus, dips may stabilize a carbon-in-mineral oil colloid, tiap may do likewise, but if applied together in a certain ratio (say dips to tiap in a molar ratio of 20 to 1), immediate flocculation may follow. In these experiments tiap was used instead of oxidation resins. The latter have a composition which is less well defined than tiap.

A few (say 1 to 10) millimoles per liter of these additives may lead to a stabilization or a flocculation of the suspension in insulating oil. If the particles in the oil are kept apart at a distance of 2ℓ ($\sim 40 \text{ \AA}$), the weak attractive forces will be influenced by soluble soaps and oxidation resins in a very small concentration, which is in sharp contrast to the conditions of stabilization and flocculation in aqueous suspensions.

Flocculation leads to a lowering of the breakdown strength, and thus the formation of soaps in the presence of an initial surplus of oxidation resins, leading to flocculation, may result in a complete breakdown of the insulating quality of the hydrocarbon oil.

At any rate, addition of a minute trace of dissociated soluble matter may easily be the cause of a marked increase in the electrical conductivity of the oil. In this respect the measurements of Van der Minne and Hermanie⁴⁾ and Koelmans⁵⁾ on liquid hydrocarbons such as mineral oil, benzene and xylene are important. In pure xylene the dissociation constant is of the order of magnitude 10^{-18} , the conductivity $< 10^{-14} \text{ ohm}^{-1} \text{ cm}^{-1}$. Addition of a non-ionic stabilizer did not cause the conductivity to increase appreciably, but addition of an ionic stabilizer such as "dips" or "tiap" of a concentration of 10 millimoles per liter increased the conductivity to a few times $10^{-10} \text{ ohm}^{-1} \text{ cm}^{-1}$, which means an increase by a factor 10^4 .

Van der Minne and Hermanie investigated the stabilization of carbon particles in lubricating oil by small amounts of aluminium naphthenate, Ca sulphanate, Ca or Mg salts of liquid resin, of phenyl stearic acid or substituted salicylic acid.

Systematic research on fine dispersions in xylene has been carried out by Koelmans⁵⁾ who used Fe_2O_3 , Al_2O_3 , SiO_2 , C, TiO_2 , CaCO_3 , BaSO_4 , Se and HgS particles having a diameter of 1 micron. Stabilizers applied were non-ionic (oleic acid, stearic acid and stearyl alcohol) or ionic (Cu oleate, tri-isoamyl-ammonium

picrate (tiap) Ca di-isopropyl salicylate (dips). The concentrations were 10 millimoles per liter and in the case of an ionic stabilizer the conductivity increased by a factor of 10^4 .

Van der Minne and Hermanie point to the low ionic concentrations necessary for a 1 : 1 electrolyte to cause or to oppose flocculation in a suspension of benzene, which is a factor 10^{-7} or 10^{-8} less than in water. In the latter a concentration of say 20–100 μ moles/l of a 1 : 1 electrolyte is required for flocculation. In benzene 400 μ moles/l of tiap is required, about 100 times less. Ionic concentrations are much lower because the degree of dissociation of the electrolyte is about 10^{-5} to 10^{-6} as against unity for water. Ionic concentrations necessary for a 1 : 1 electrolyte to cause flocculation in benzene are therefore 10^{-7} to 10^{-8} times less than in water.

The mechanism will be quite different in the two cases; the concept of compression of the double sheath assumed for water, is entirely out of the question at the low concentrations occurring in benzene.

§. 4. *Inhibitors.* If bridges are being formed in the oil, deterioration takes place due to local heating in the bridges, by which gas bubbles and carbon particles may be formed. In these gas bubbles corona discharges take place, by which (in the presence of oxygen) acids may be formed. Those corona discharges and the formation of carbon may be prevented by keeping the colloid particles small and dispersed. Formation of bridges is then impossible.

It has been shown in § 2 that aromatic molecules are surface-active towards carbon particles. A number of synthetic aromatic inhibitors may be added to supply a protective cover around carbon particles, protecting them against further flocculation. It is not by chance that dye research has supplied a great number of inhibitors to the constructors of cables, transformers and capacitors (anthraquinone). An extensive review of this subject has been compiled by Callinan ⁶).

Mineral oil may contain a large proportion of aromatic compounds possessing long aliphatic side chains. It has become clear that purification of mineral oil should not lead to a removal of these natural inhibitors, as has been pointed out by Imhof ⁷). The oil may deteriorate rapidly if the purification has gone too far.

Carbon particles in aromatic liquids are kept dispersed and do not flocculate rapidly. The stability of a synthetic aromatic compound such as chlorinated diphenyl is clear.

§ 5. *Liquids free from inhibitors.* The author carried out an experiment in which any stabilizing influence was assumed to be absent. In twice-distilled carbon tetrachloride a carbon sol was prepared by effectuating a number of electrical breakdowns. A sol of brownish hue ensued. After a few minutes the carbon particles in a drop of the liquid on a glass plate were found by microscopic observation to grow to larger complexes which even became visible to the naked eye.

In this case no stabilization could take place. Evidently carbon tetrachloride should be considered to be less suitable as an insulating liquid, although the flow of the coarsening carbon particles through the pores of insulating paper may be relatively slow or even completely impossible.

Received 27th October, 1960.

REFERENCES

- 1) Kok, J. A. and M. M. G. Corbey, *Appl. Sci. Res. B* **7** (1958) 257.
- 2) Overbeek, J. Th. G., see H. R. Kruyt, *Colloid Science I*, Elsevier 1952, 58-89, 264-266; H. C. Hamaker, *Physica* **4** (1937) 1058; Verwey, E. J. W. and J. Th. G. Overbeek, *Theory of the Stability of Lyophobic Colloids*. Elsevier, 1948.
- 3) Mysels, K. J., *Introduction to Colloid Chemistry*, p. 176-206, Interscience Publ. Inc., N. York and London, 1959; J. P. Sisley and P. J. Wood, *Encyclopedia of surface-active agents*, Chemical Publishing Co. Inc., N. York 1952; A. M. Schwartz, J. W. Perry (and J. Berch), *Surface active agents (and detergents) I (and II)*, Intersc. Publ. Inc., N. York and London, 1949 and 1958.
- 4) Minne, J. L. van der, *Rec. Trav. chim.* **65** (1946) 549; J. L. van der Minne and P. H. J. Hermanie, *J. Colloid Sci.* **8** (1953) 38; **7** (1952) 600; M. van der Waarden, *J. Colloid Sci.* **5** (1950) 317, 448; **6** (1951) 443; E. L. Mackor and J. H. van der Waals, *J. Colloid Sci.* **7** (1952) 535; E. L. Mackor, *J. Colloid Sci.* **6** (1951) 492.
- 5) Koelmans, H., *Philips Res. Rep.* **10** (1955) 161.
- 6) Callinan, Th. D., *Electrical insulation and dielectrics*, 1955, p. 70, *An electrical manufacturing design manual*, Gage Publ. Co., N. York.
- 7) Imhof, A., *Hochspannungs-Isolierstoffe*, G. Braun, Karlsruhe, 1957.

MAGNETIC MEASUREMENTS ON PURE MnCO_3 , PURE MnO AND DISSOCIATING MnCO_3

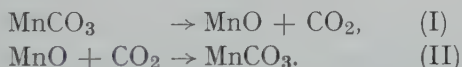
by J. A. POULIS, C. H. MASSEN and P. VAN DER LEEDEN

Technological University, Eindhoven, Netherlands

Summary

With a sensitive susceptibility balance measurements have been carried out on dissociating MnCO_3 . The magnetic susceptibility of pure MnCO_3 , which was the initial material, proved to follow the Curie-Weiss law; pure MnO , as a result of the complete dissociation, showed deviations from this law. The recombination of MnO with the collected CO_2 was studied, the results leading to a hypothesis concerning the reaction mechanism of dissociation and recombination.

§ 1. *Introduction.* Measurements are reported of the magnetic susceptibilities of pure MnCO_3 , pure MnO and of the solid products of MnCO_3 , dissociated in different degrees. The ratio of MnCO_3 and MnO in the sample was varied by means of the following chemical reactions:



Our aim was to collect data about the magnetic behaviour of the pure substances as well as to study the reactions (I) and (II).

For measuring magnetic susceptibilities according to Faraday's method we used a torsion balance, its deviations being determined with an electronic displacement meter. To test the reliability of the apparatus during several weeks, a diamagnetic substance was mounted in a rather weak magnetic field (3000 Oe). The magnetic force measured by our balance was reproduced better than 0.1%. Readjustment of the probe caused a deviation of the order of 1%. To avoid the influence of such a disturbance of the balance, we let the reactions proceed in a container which was permanently

attached to the balance during the whole experiment. Therefore the original pure MnCO_3 was put in a glass bulb, having a connection with a much larger one in which the CO_2 was stored; both bulbs were attached to the balance. The first glass bulb could move in a small furnace placed between the pole pieces of the magnet while the bulb containing the CO_2 was placed outside both furnace and magnetic field. When the temperature is raised, reaction I dominates, while lowering of the temperature favours reaction II. So we could vary the dissociation ratio.

As neither of the susceptibilities of the pure solids is better known than 1% and on the other hand calibration of our balance with a better known substance also brought along a comparable error, the accuracy of 0.1%, as suggested by the data given, has significance only for the relative values of all the data presented in this paper.

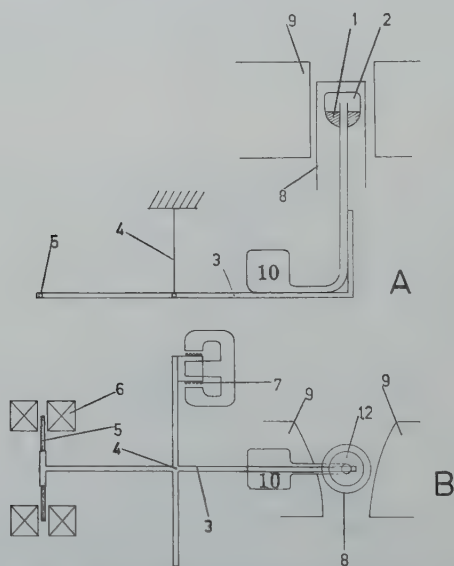


Fig. 1. A) Vertical en B) horizontal view of the apparatus (schematically).
For the meaning of the symbols see text.

§ 2. *Apparatus.* The apparatus is shown schematically in fig. 1. Two crossed bars are suspended from a platinum-nickel strip 4. The sample was mounted on the end of the first bar 3. The moving part of the displacement meter was attached to the opposite end

of this bar. One end of the other bar was connected to a compensating-force unit, while the remaining end only served for balance. The sample was put into an initially evacuated glass bulb 2 moving inside a furnace 8, which was mounted between the pole pieces of a small electromagnet 9.

The pole pieces were designed in such a way that the differences between values of $H \partial H / \partial x$ over the whole area of the field in which the sample moved were sufficiently small. The CO_2 formed by the reaction I was gathered in the glass bulb 10 outside the furnace and the magnetic field.

The moving part of the displacement meter consisted of two ferroxcube rods 5. These could move in and out of two coils 6. The ratio of the coefficients of selfinduction was measured by means of an impedance bridge. When this ratio did not vary any more, the forces on the balance were taken to be in equilibrium. The compensating-force unit consisted of a coil 7 moving in the field of a permanent magnet, the current through the coil being varied until the induced Lorentz force compensated the magnetic force on the sample.

§ 3. *Measurements.* Measurements were started on a sample of MnCO_3 in the evacuated bulb. The curve of the susceptibility of MnCO_3 versus temperature was measured several times. This curve is shown in fig. 2 (curve I). These data and all susceptibility data following in this paper have been corrected for the diamagnetism of the glass bulb, for the paramagnetism of the surrounding air and also for the diamagnetic part of the susceptibility of the sample. As long as 370°C was not surpassed, this curve reproduced. As we did not expect any equilibria that would adapt swiftly to a dissociation degree corresponding to the temperature, we concluded that no dissociation had taken place so far. When the temperature was raised above 370°C , dissociation started according to reaction I. This was concluded from the variations of the measured susceptibility at constant temperature.

When after a dissociation period at a temperature above 370°C the sample is kept at temperature below 370°C , recombination occurs according to reaction II. This recombination was thoroughly studied at room temperature. In order to obtain information concerning the dependence of the susceptibility of mixtures of

MnCO_3 and MnO on the temperature during the recombination at room temperature, short interruptions were introduced several times. During each interruption the temperature was raised up to about 300°C and lowered again to room temperature. The susceptibility measurements taken while raising the temperature were plotted and a curve was drawn through the points. Data gathered during the lowering of the temperature corresponded to points belonging to the same curve. This led to the conclusion that these interruptions did not affect the structure of the mixture, thus allowing to determine its χ - T -curve. Several subsequent dissociations and recombinations were carried out with the same sample.

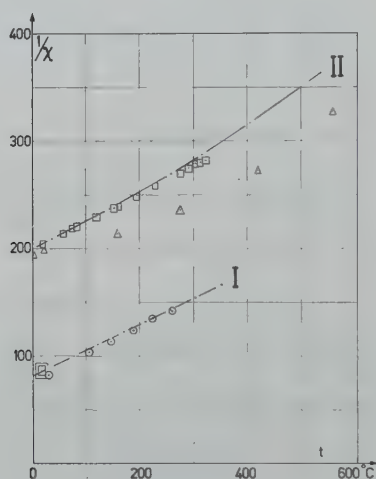


Fig. 2. Inverse susceptibilities versus temperature for MnCO_3 (curve I) and MnO (curve II). The lines drawn connect our own measurements. Other points are from \circ Krishnan¹, \square Bizette⁴, \square Birckel², \triangle Honda³).

The last dissociation period was taken at 500°C . This temperature was maintained until the susceptibility remained constant, indicating that the whole sample was transformed into MnO . This complete dissociation was checked by further raising of the temperature, no indication of a further dissociation being found in this way. Later on we got another check by X-ray analysis. The susceptibility of this MnO is plotted as a function of temperature in fig. 2 (curve II). These measurements were taken in a similar way as described above. Again the curve proved reproducible. This curve too will

be discussed later on. With the help of the susceptibility curves of pure MnO and pure MnCO_3 we are now able to calculate the dissociation ratio of our sample at any time of the experiment. This can be done at every temperature by presupposing linear additivity of the susceptibilities of the components at that temperature. The complete experiment can now be described with the help of fig. 3. In this figure, the ratio of dissociation during the whole experiment is plotted against time.

Several dissociation ratios plotted there were calculated from susceptibility measurements at different temperatures between room temperature and 370°C without any indication of the temperature influencing the dissociation ratio during the short time of measuring as explained before. The heating periods during which dissociation occurred, can be found as discontinuities of the curve in fig. 3.

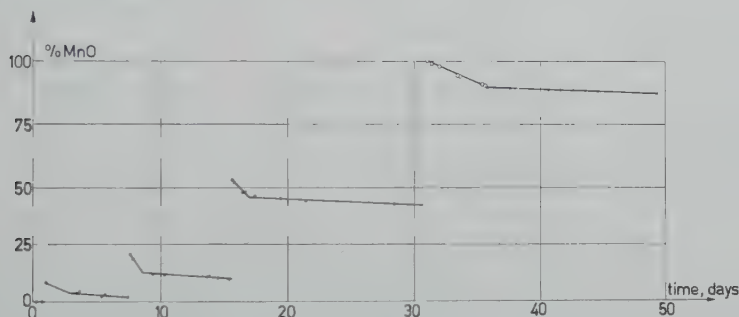


Fig. 3. The dissociation ratio versus the time throughout the whole experiment; points are measured during recombinations at room temperature, except points given by the symbol \circ which were drawn during recombination at 250°C .

The form of the recombination curves indicates that two processes with quite different time constants play a role. The dissociation period is always directly followed by a relatively fast recombination of limited extent and duration, and later on by a relatively slow recombination. A part of the last recombination was carried out at 250°C .

§ 4. Results and discussion.

I. The temperature dependence of the susceptibility of MnCO_3 . According to the Curie-Weiss-law the $1/\chi - T$ curve

for a paramagnetic substance should be a straight line, given by

$$\frac{1}{\chi} = \frac{14.05^2}{P_w^2} (T - \theta),$$

where P_w is the magnetic moment of the paramagnetic ion expressed in Weiss magnetons and θ a constant characteristic for the substance.

In fig. 2 (curve I) the results of our measurements after corrections mentioned previously in this paper are plotted. Our graph shows a straight line in the case of MnCO_3 . From the separate points we calculated the constants P_w , using the method of least squares:

$$P_w = 28.74 \pm 0.09, \quad \theta = -71.4 \pm 3.5^\circ\text{K}.$$

The given uncertainties are estimated standard errors. For comparison we give the results of resp. Krishnan ¹⁾ and of Birckel ²⁾ for MnCO_3 :

$$\begin{array}{ll} \text{Krishnan:} & P_w = 27.5 \pm 1.8, \quad \theta = -13^\circ \pm 60^\circ\text{K}; \\ \text{Birckel:} & P_w = 28.0 \pm 0.25, \quad \theta = -56^\circ \pm 9^\circ\text{K}. \end{array}$$

Significant incompatibilities do not occur.

II. The temperature dependence of the susceptibility of MnO . In fig. 2 (curve II) our measurements concerning MnO are given and compared with those of Honda ³⁾ and of Birckel ²⁾. The deviations from the Curie-Weiss-law, suggested by the results of Honda, became doubtful after the work of Birckel; they are however significant according to our measurements. Recently results concerning the susceptibility of MnS have been published ⁵⁾. Here similar deviations from the Curie-Weiss-law are stated.

We tried to describe our results by putting $1/\chi$ equal to a quadratic polynomial in T and determining the three constants by the method of least squares. The discrepancy between the curve thus found and the measured points could be described by a standard error of 0.08%. Deviation from a straight line would be systematic and amount to about 5%. A study of these discrepancies taught that higher than second order approximations could not be expected to give a significantly better description.

Values of P_w were calculated at various temperatures by using

the Curie-Weiss-law for the tangent (fig. 4). The values of P_w plotted in fig. 4 below room temperature were the result of extrapolation of our polynomial. They show the quite remarkable fact that near the Néel temperature the number of magnetons of MnO is equal to the theoretical number $P_w = 29.3$ corresponding to $S = 5/2$.

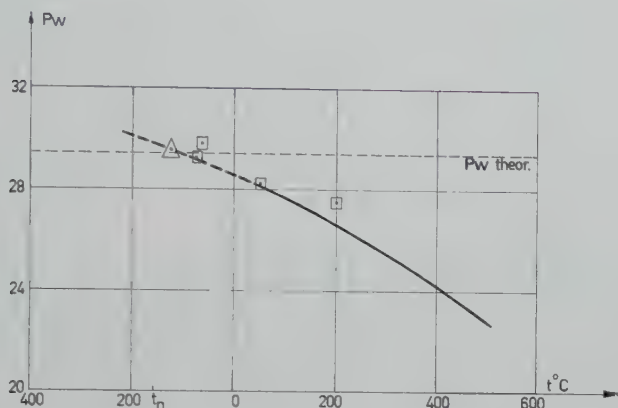


Fig. 4. The temperature dependence of the number of Weiss magnetons of MnO versus temperature. The line drawn connects our own measurements, the dotted line is an extrapolation. The other points are measured by □ Birckel²⁾, Δ Bizette⁴⁾.

III. The reactions. From our magnetic measurements in conjunction with X-ray and microscopic investigations some conclusions about the reaction mechanisms may be drawn.

Microscopical observations showed that the grain sizes were the same before and after the measurements described in fig. 3. The X-ray investigations showed that we had to do with large and small crystals of both MnO and MnCO_3 . The large crystals ($> 500 \text{ \AA}$) gave sharp diffraction lines while the small crystals ($\sim 300 \text{ \AA}$) gave broader ones, which were displaced a bit, due to the lattice constants being influenced by the size of the crystals. X-ray investigations have been made before and after the measurements of fig. 3. At several intermediate points X-ray information was drawn from a similar sample, which was given the same heat treatment.

The X-ray experiments showed that the original MnCO_3 con-

sisted of large crystals. After each heating period 9% of the total amount of Mn ions formed small MnO crystals. The fast part of a recombination resulted in the formation of 9% of small crystals of MnCO_3 and elimination of the small MnO crystals.

This led us to the following suggestion about the reaction mechanism: An original MnCO_3 grain consists of large crystals. By heating, the surface layer the grain can easily be dissociated; small MnO crystals are formed. The central part of the grain can only be affected by more extensive heating.

The small MnO crystals in the surface layer when in contact with CO_2 gas at room temperature can easily recombine to form small crystals of MnCO_3 , the MnO crystals at the inside of the grain recombine much more slowly.

Acknowledgement. The X-ray analyses were partly done at the laboratory of T.N.O., Delft. Thanks are due to A. G. M. L. Weyts and H. G. de Winter for their discussions of the manuscript.

Received 12th December, 1960.

REFERENCES

- 1) Krishnan, K. S. and S. Banerjee, Z. Krist. **99** (1938) 499.
- 2) Birckel, A., Cahiers Phys. No. **25** (1944) 45.
- 3) Honda, K. and T. Soné, Sci. Rep. Tôhoku Imp. Univ. First Ser. **3** (1944) 139.
- 4) Bizette, H., C. F. Squire and B. Tsai, C.R. Acad. Sci., Paris **207** (1938) 449.
- 5) Banewicz, J. J., K. F. Heidelberg and R. Lindsay, Phys. Rev. **117** (1960) 736.

COUETTE FLOW OF A FULLY IONIZED GAS, CONSIDERED AS A TWO-COMPONENT FLUID

by L. A. PELETIER *) and L. VAN WIJNGAARDEN

Mededeling No. 94 uit het Laboratorium voor Aero-en Hydrodynamica van de
Technische Hogeschool te Delft, Netherlands

Summary

The equations, governing the behaviour of a fully ionized gas, as given by Spitzer, are applied to two types of magnetohydrodynamic Couette flow. The features of the flow are expressed in terms of the Hartmann number and a parameter q , being the ratio between Larmor frequency and collision frequency. Compared with the results of the one-component theory an additional velocity component is found.

§ 1. *Introduction.* In dealing with problems concerning the motion of an ionized gas through a magnetic field one may consider the gas to be continuous as long as the mean collision frequency is large with respect to the gyration frequency of the motion of charged particles about the lines of magnetic induction.

When the ratio between gyration frequency and collision frequency is not negligibly small, additional effects must be taken into account. This is done, following Spitzer¹⁾ by considering a fully ionized gas as a mixture of two components, one consisting of positively and the other of negatively charged particles. From the equations of motion of the two components the equations governing the macroscopic velocity and current density of the gas can be deduced.

In § 2 we apply Spitzer's equations, extended with a viscous term, to the flow of a viscous fully ionized gas between two parallel infinite plates, one being at rest and the other moving with a constant velocity. A constant magnetic field is applied in the direction normal to the plates. We consider two different cases of

*) At present at the Massachusetts Institute of Technology, Cambridge Mass. U.S.A.

this Couette-flow. In § 3 the fluid is shortcircuited parallel to the plates whilst in § 4 both plates are insulators.

A velocity component, not present in the one-component theory, perpendicular to the normal to the plates and the velocity of the moving plate is found. An additional shear force in that direction results from this velocity component. This effect is shown to be related to that noticed by Broer and the present authors²⁾ in studying the forced motion of a non-viscous fully ionized gas between two parallel plates at rest.

§ 2. *Equations for Couette-flow in two-component theory.* Consider two parallel plates of infinite length and width. One of them coincides with the x^*z^* plane, is at rest and is a perfect conductor. The other one, a non-magnetic insulator, moves at $y^* = h$ with a constant velocity U in the direction of the positive x^* axis. Outside the plates is a constant homogeneous magnetic field directed along the positive y^* axis.

The space between the plates is occupied by a fully ionized viscous gas, consisting of protons and electrons. Moreover we assume the gas as a whole to be neutral and in thermal equilibrium. It is assumed that U is low enough to make compressibility effects negligible. We seek the velocity distribution in the gas and the forces on the plates, when the equations of Spitzer's two-component theory are applied to the motion engendered by the moving plate.

First we have to consider that the equations given by Spitzer (ref.1), p. 21) result from the linearized equations of motion of the components, and that they give no account of viscosity. The first point gives no difficulty because the convective acceleration, neglected by Spitzer, vanishes in our case as all quantities depend only on y^* .

As for viscosity, Spitzer's equations can be extended to viscous problems by introducing in the equation of motion the viscous term of the Navier-Stokes equation. Doing this we have, bearing in mind that the motion is steady (in M.K.S. units):

$$\mathbf{J} \times \mathbf{B} - \nabla P + \eta \nabla^2 \mathbf{v} = 0 \quad (1)$$

and

$$\mathbf{E}^* + \mathbf{v} \times \mathbf{B} - \frac{\mathbf{J}}{\sigma} = \frac{\mathbf{J} \times \mathbf{B}}{en} - \frac{\nabla P}{2en}, \quad (2)$$

where

\mathbf{v} = velocity

\mathbf{B} = magnetic induction

P = pressure

\mathbf{E}^* = electric field strength

e = charge of proton

n = number of particles of each component in a m^3

σ = electrical conductivity

\mathbf{J} = current density

η = coefficient of viscosity.

(1) and (2) differ from the corresponding equations in the one-component theory by the terms on the right-hand side of (2). They represent the influence of the Hall-current and the partial electron pressure respectively. In the one component theory the right hand side of (2) is zero giving Ohm's law. It can be made plausible that in (2) viscous terms can be neglected, the electronic contribution to viscosity being very small (cf. Chapman ³).

In addition to (1) and (2) we have

$$\nabla \cdot \mathbf{v} = 0, \quad (3)$$

$$\nabla \cdot \mathbf{B} = 0, \quad (4)$$

$$\nabla \times \mathbf{E}^* = 0, \quad (5)$$

$$\nabla \times \mathbf{B} = \mu \mathbf{J}, \quad (6)$$

where μ is the magnetic permeability. In order to formulate the problem in terms of dimensionless quantities we take

$$x^* = xh, y^* = yh, z^* = zh, \mathbf{v} = \mathbf{u}U, \mathbf{B} = \mathbf{b}B_0,$$

$$\mathbf{E}^* = \mathbf{E}UB_0, \mathbf{J} = \mathbf{j}\sigma UB_0, P = p \frac{\eta U}{h}.$$

Then (1)–(6) become

$$M^2 \mathbf{j} \times \mathbf{b} - \nabla p + \nabla^2 \mathbf{u} = 0, \quad (7)$$

$$\mathbf{E} + \mathbf{u} \times \mathbf{b} - q \mathbf{j} \times \mathbf{b} - \mathbf{j} = 0, \quad (8)$$

$$\nabla \cdot \mathbf{u} = 0, \quad (9)$$

$$\nabla \cdot \mathbf{b} = 0, \quad (10)$$

$$\nabla \times \mathbf{E} = 0, \quad (11)$$

$$\nabla \times \mathbf{b} = R_m \mathbf{j} \quad (12)$$

These equations contain three dimensionless groups:

$$M = B_0 h \left(\frac{\sigma}{\eta} \right)^{\frac{1}{2}}, \quad R_m = \mu \sigma U h, \\ q = \frac{\sigma B_0}{en}. \quad (13)$$

M is the Hartmann number, R_m the magnetic Reynolds number, while q is the ratio mentioned in the introduction. This is easily seen by remembering that kinetic theory gives $\sigma = e^2 n \tau / m$, where τ is the mean collision time for collisions between electrons and protons and m is the mass of an electron. Upon inserting this in (13) we obtain $q = \omega \tau$, where $\omega = e B_0 / m$ is the frequency of gyration about the lines of magnetic force for an electron.

The quantity q measures the number of rotations about lines of magnetic induction which an electron performs between collisions with protons. Here we must restrict ourselves to small values of q as (1) and (2) are valid only for this case. For larger values of q the quantities σ and η cannot be represented by scalars.

Next we have to formulate the boundary conditions. They must state that there is no slip at the plates, that no electric current is flowing into the upper plate, this being an insulator, that the y -component of the magnetic induction is continuous at both plates and that the other components are continuous at the upper plate since this one carries no current.

Hence we have

$$y = 0: \quad u = 0, \quad b_y = 1,$$

$$y = 1: \quad u_x = 1; \quad u_y = u_z = 0, \quad j_y = 0, \quad b_y = 1; \quad b_x = b_z = 0.$$

From the boundary conditions and (9)–(12) we deduce, keeping in mind that there is only dependance on y :

$$u_y = 0, \quad b_y = 1, \quad j_y = 0, \quad E_z = \text{constant}, \quad E_x = \text{constant}.$$

Using these results, the x and z components of (7) become

$$-M^2 j_z + \frac{d^2 u_x}{dy^2} = 0, \quad (14)$$

$$M^2 j_x + \frac{d^2 u_z}{dy^2} = 0, \quad (15)$$

and of (8)

$$E_x - u_z + q j_z - j_x = 0, \quad (16)$$

$$E_z + u_x - j_z - q j_x = 0. \quad (17)$$

Solution of (14)–(17) requires the knowledge of six constants, including E_z and E_x . The boundary conditions for \mathbf{u} give us four relations between these constants. Hence two additional relations are needed. In the next two paragraphs two different choices for these relations are made.

§ 3. *Shortcircuited gas.* We suppose the gas to be shortcircuited in the x and z direction. This implies

$$E_x = E_z = 0. \quad (18)$$

It is possible to solve (14)–(17) together with the boundary conditions and (18) for all values of q . But, as already indicated, the validity of the present theory is restricted to small values of q . Therefore we give here the solution for small q . When neglecting terms of second order in q , we obtain from (16) and (17) with help of (18)

$$u_z = qu_x - j_x \quad (19)$$

or with (15)

$$u_z = qu_x + \frac{1}{M^2} \frac{d^2 u_z}{dy^2}. \quad (20)$$

The first term at the right-hand side of (20) is related to a result obtained by Broer and the present authors²⁾. They studied the motion of a non-viscous fully ionized gas between two infinite parallel plates, a constant magnetic field being applied normal to the plates. In their problem the motion is caused by a constant volume-force. It was shown that the gas moves at an angle φ with respect to the direction of the driving force where φ is given by $\tan \varphi = \frac{1}{2}q$. In the present problem the driving force is the x -component of the viscous stress. The first term at the right-hand side of (20) shows that a similar effect is present here. The second term represents the influence of the shear stress in the z -direction on the drift velocity u_z . From (19) we deduce that j_x is of the first order in q . Hence we obtain from (17) and (18) that in our approximation $u_x = j_z$. Inserting this in (14), yields

$$\frac{d^2 u_x}{dy^2} - M^2 u_x = 0. \quad (21)$$

Obviously there is no influence of q on u_x up to the second order.

The solution of (21) satisfying the conditions

$$y = 0: u_x = 0, \quad y = 1: u_x = 1$$

is

$$u_x = \frac{\sinh My}{\sinh M}. \quad (22)$$

With the help of (22) and the boundary conditions

$$y = 0: u_z = 0, \quad y = 1: u_z = 0$$

the solution of (20) is

$$u_z = \frac{Mq}{2 \sinh^2 M} (\cosh M \sinh My - y \cosh My \sinh M). \quad (23)$$

For large M , i.e.

$$\cosh M \approx \sinh M \gg M \gg 1, \quad (24)$$

we can approximate (22) and (23) for $y > 0$ by

$$u_x \approx \exp[-M(1-y)], \quad (25)$$

$$u_z \approx \frac{1}{2}Mq(1-y) \exp[-M(1-y)]. \quad (26)$$

These expressions show that for large M the motion is restricted to a boundary layer on the upper plate (whose thickness is of order $1/M$), the ratio u_z/u_x in this boundary layer being given by

$$u_z/u_x \approx \frac{1}{2}Mq(1-y).$$

Once u_x and u_z are known, \mathbf{j} can be calculated from (14) and (15), \mathbf{b} from (12), E_y and dp/dy from the y -components of (7) and (8). As these quantities are of no great interest, we don't give them here. We only mention that the two integration constants involved in the calculation of b_x and b_z from (12) are determined by the conditions that b_x and b_z must be zero at the upper plate. The values of b_x and b_z at the lower plate then determine the current in the lower (perfect conducting) plate. This current is equal and opposite to the total current in the gas.

Quantities of interest are the viscous stresses exerted at the plates. They are given in dimensionless form by the first derivatives at the plates of u_x and u_z . Denoting these dimensionless stresses

by k_x and k_z we have, from (22) and (23) at the lower plate,

$$k_x = \left(\frac{du_x}{dy} \right)_{y=0} = \frac{M}{\sinh M},$$

$$k_z = \left(\frac{du_z}{dy} \right)_{y=0} = \frac{Mq}{2 \sinh^2 M} (M \cosh M - \sinh M),$$

and at the upper plate,

$$k_x = - \left(\frac{du_x}{dy} \right)_{y=1} = -M \coth M, \quad (27)$$

$$k_z = - \left(\frac{du_z}{dy} \right)_{y=1} = \frac{Mq}{4 \sinh^2 M} (\sinh 2M - 2M). \quad (28)$$

In the case where M is large (24), (27) and (28) yield for the ratio between k_z and k_x at the upper plate

$$k_z/k_x = -\frac{1}{2}q. \quad (29)$$

The expression (29) resembles the expression obtained by Broer *et al.*, in their already cited note, for the mechanical Hall-effect, i.e. the pressure gradient build up perpendicular to the driving force, when in their problem the gas is compelled, by walls inserted in the flow, to move parallel to the driving force. This pressure gradient was found to be $\frac{1}{2}q$ times the (volume) force.

§ 4. *Insulated plates.* We return to equations (14)–(17) and assume now that both plates are insulators, electrically and magnetically. Hence the net current in the gas is zero:

$$\int_0^1 j_x dy = 0, \quad \int_0^1 j_z dy = 0.$$

With these conditions we obtain from (14) and (15) upon integration between 0 and 1:

$$\left(\frac{du_x}{dy} \right)_{y=0} = \left(\frac{du_x}{dy} \right)_{y=1}, \quad (30)$$

$$\left(\frac{du_z}{dy} \right)_{y=0} = \left(\frac{du_z}{dy} \right)_{y=1}. \quad (31)$$

The solution of (14)–(17) then has to satisfy (30), (31) and the conditions for \mathbf{u} given in § 3.

Here again we consider only small values of q . Neglecting terms of second order in q , we obtain, using the same arguments as in the foregoing paragraph,

$$u_z = qv_x + \frac{1}{M^2} \frac{d^2 u_z}{dy^2} + E_x + qE_z \quad (32)$$

and

$$\frac{1}{M^2} \frac{d^2 u_x}{dy^2} - u_x = E_z. \quad (33)$$

The solution of (33), satisfying

$$y = 0: u_x = 0, \quad y = 1: u_x = 1,$$

and (30) is

$$u_x = \frac{1}{2} \left[1 + \frac{\sinh M(y - \frac{1}{2})}{\sinh \frac{1}{2}M} \right], \quad (34)$$

$$E_z = -\frac{1}{2}. \quad (35)$$

Substituting (34) and (35) into (32), we find using (31) and the conditions

$$y = 0: u_z = 0, \quad y = 1: u_z = 0,$$

the following expression for u_z :

$$u_z = \frac{Mq}{4 \sinh^2 \frac{1}{2}M} \cdot \left[\frac{1}{2} \cosh \frac{1}{2}M \sinh M(y - \frac{1}{2}) - (y - \frac{1}{2}) \sinh \frac{1}{2}M \cosh M(y - \frac{1}{2}) \right], \quad (36)$$

whilst $E_x = 0$.

When we move the x^* -axis to $y^* = \frac{1}{2}h$ in the dimensional coordinate system, then the ordinate is $y^{*'} = y^* - \frac{1}{2}h$. Upon choosing

$$\zeta = \frac{y^{*'}}{\frac{1}{2}h}$$

we have

$$y - \frac{1}{2} = \frac{y^{*'} + \frac{1}{2}h}{h} - \frac{1}{2} = \frac{1}{2}\zeta.$$

Inserting this into (34) and (36) yields

$$u_x - \frac{1}{2} = \frac{1}{2} \frac{\sinh \frac{1}{2} M \zeta}{\sinh \frac{1}{2} M}, \quad (37)$$

$$u_z = \frac{Mq}{8 \sinh^2 \frac{1}{2} M} [\cosh \frac{1}{2} M \sinh \frac{1}{2} M \zeta - \zeta \sinh \frac{1}{2} M \cosh \frac{1}{2} M \zeta]. \quad (38)$$

Comparison of these expressions with (22) and (23) shows that in the region $0 \leq \zeta \leq 1$ the expressions for $(u_x - \frac{1}{2})$ and u_z as given by (37) and (38) are the same as the corresponding ones obtained in the foregoing paragraph, provided we assume in § 3 the distance between the plates to be $\frac{1}{2}h$ instead of h and the velocity of the upper plate $\frac{1}{2}U$ instead of U .

This similarity and the antisymmetry of the right-hand sides of (37) and (38) with respect to $\zeta = 0$, enables us to obtain all quantities from the corresponding ones in § 3 by applying the scaling rules mentioned above. To obtain the stresses on the plates we have only to replace M by $\frac{1}{2}M$ in (27) and (28). Then we have from (27) and (28) in view of the antisymmetry

$$k_x = \pm \frac{1}{2} M \coth \frac{1}{2} M,$$

$$k_z = \pm \frac{Mq}{8} \left(\frac{M - \sinh M}{\sinh^2 \frac{1}{2} M} \right),$$

where $+$ refers to the lower and $-$ to the upper plate. Clearly, there is no net force, in agreement with the fact, that the net current vanishes.

When M is large there is a boundary layer on each plate; (37) and (38) together with (24) give for the velocity distribution in the boundary layers

$$u_x - \frac{1}{2} \approx \frac{1}{2} \exp[-\frac{1}{2} M (\pm \zeta + 1)],$$

$$u_z \approx \frac{Mq}{8} (\pm \zeta + 1) \exp[-\frac{1}{2} M (\pm \zeta + 1)],$$

where again $+$ refers to the lower and $-$ to the upper plate. In § 3 we obtained the expression (29) for the ratio between k_z and k_x at the upper plate when M is large. (29) does not contain M and therefore holds here too. Hence we have at both plates $k_z/k_x = -\frac{1}{2}q$ when M is large.

Acknowledgement. The authors would like to express their thanks to Prof. dr. L. J. F. Broer for his interest and for many helpful suggestions.

Received 15th November, 1960.

REFERENCES

- 1) Spitzer, L. jr., *Physics of fully ionized gases*. Interscience Publishers, Inc. New York 1956.
- 2) Broer, L. J. F., L. A. Peletier and L. van Wijngaarden, *Appl. Sci. Res. B* **8** (1960) 259.
- 3) Chapman, S., *Astrophys. J.* **120** (1954) 151.

ELECTROSTATIC DIPOLE MOMENT OF A DIELECTRIC CUBE

by T. W. EDWARDS and J. VAN BLADEL

Department of Electrical Engineering,
University of Wisconsin, Madison, Wisconsin, U.S.A.

Summary

The electrostatic dipole moment of a dielectric cube introduced into a uniform electrostatic field can be determined by solving an appropriate surface integral equation. High-speed digital computers have been employed to solve the matrix approximation to this equation.

§ 1. *Introduction.* The dipole moment of a dielectric body introduced into a known electrostatic field can be calculated by separation of variables for a few simple shapes such as the cylinder, the sphere, and the ellipsoid. However, there exists a surface integral equation method of calculating the dipole moment which is valid for all shapes. The actual solution of this integral equation must be effected by approximate methods of considerable complexity. The advent of modern high-speed digital computers permits solution of many problems previously intractable. The authors decided to apply these methods to the solution of the dipole problem. For the sake of simplicity, a cubical shape in a uniform field was chosen. The results obtained are applicable to the scattered field of a dielectric cube immersed in a plane wave whose wavelength is large compared with the dimensions of the cube.

§ 2. *The integral equation.* Phillips¹⁾ has shown that the electrostatic potential distribution ϕ inside and outside a dielectric body inserted into a pre-existing potential distribution ψ (see fig. 1) can be expressed, respectively, in terms of the resulting surface

potential distribution by the formulae

$$\kappa\phi(P_i) = \psi(P_i) + \frac{1-\kappa}{4\pi} \iint_S \phi(p) \frac{\partial}{\partial n_p} \frac{1}{|\bar{r}_p - \bar{r}_{P_i}|} dS_p, \quad (1)$$

$$\phi(P_e) = \psi(P_e) + \frac{1-\kappa}{4\pi} \iint_S \phi(p) \frac{\partial}{\partial n_p} \frac{1}{|\bar{r}_p - \bar{r}_{P_e}|} dS_p, \quad (2)$$

where κ is the dielectric constant of the body.

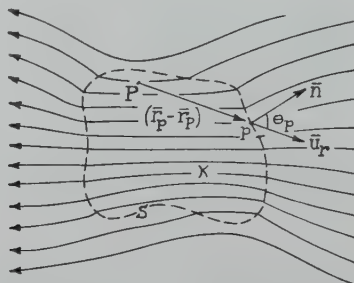


Fig. 1. A dielectric body bounded by the surface S .

Allowing the points P_i and P_e to approach a point P_0 on the surface S of the dielectric body leads to the following integral equation for the surface distribution:

$$\psi(p_0) = \frac{\kappa+1}{2} \phi(p_0) + \frac{\kappa-1}{4\pi} \iint_S \phi(p) \frac{\partial}{\partial n_p} \frac{1}{|\bar{r}_p - \bar{r}_{P_0}|} dS_p. \quad (3)$$

§ 3. *Specialization to a dielectric cube immersed in a uniform electrostatic field.* The dipole moment of the cube obviously depends on the orientation of the cube with respect to the direction of the initial uniform field \mathbf{E}_0 . However, by separating the field into its three components, each normal to a pair of faces of the cube, it is seen that the problem reduces to the calculation of the dipole moment induced by any one of the three components.

Thus, considering the z orientation only (see fig. 2), the original potential distribution ψ is given by

$$\psi = E_0 z. \quad (4)$$

The surface integrals in (1), (2) and (3) may be approximated by finite sums by dividing each face of the cube, of total area $4a^2$, into N^2 equal sections, and by considering the potentials ϕ and ψ to be constant over each section. In this manner (3) gives rise to

a matrix equation

$$[\psi(p_0)] = \frac{\kappa + 1}{2} [\phi(p_0)] + \frac{1 - \kappa}{\pi} [A][\phi(p)], \quad (5)$$

where $[A]$ is a square matrix of order Q . Consideration of the symmetry properties of the surface potential distribution $\phi(p)$ reduces the order of Q and the number of unique values of potential

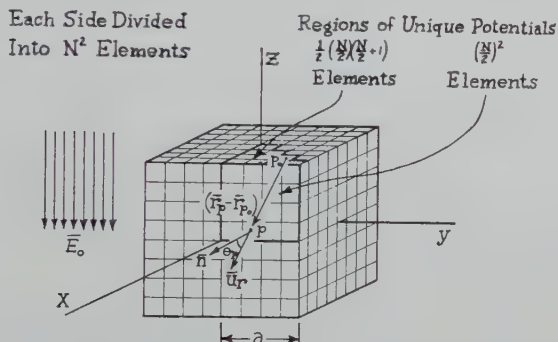


Fig. 2. A dielectric cube immersed in an otherwise uniform electrostatic field.

from $6N^2$ to (when N is even) $3N^2/8 + N/4$. The storage capacity of the computer employed (an IBM 650) limited the maximum usable value of N to 10, i.e. $Q = 40^*$). Obviously, the matrix approximation to the integral equation improves in accuracy as N increases.

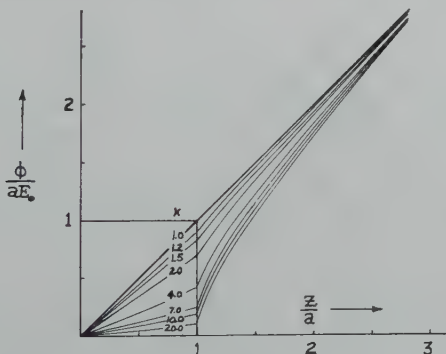


Fig. 3. Total potential distribution (along the z axis) of a dielectric cube. Note that, in this and succeeding figures, the properties of the cube approach those of a metallic cube, as the dielectric constant κ increases indefinitely.

^{*}) For more details on the establishment of (5) and for details of the computational program, see ²⁾.

Fig. 3 shows the total potential distribution along an axis through the centre of the cube and extending in the direction of the initial field. Fig. 4 shows the fraction of this potential distribution due to the presence of the dielectric cube.

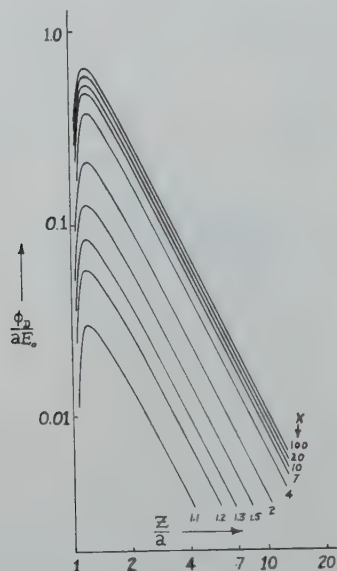


Fig. 4. Dipole potential distribution (along the z axis) of a dielectric cube.

§ 4. *Dipole moment.* The dipole moment of the dielectric cube can be read directly from fig. 4, where the $1/R^2$ decrease of the potential at large distance is evident. It can also be determined from the definition of the dipole moment \mathbf{P} and from (2) as

$$\phi_{\text{Dipole}} = \frac{\mathbf{P} \cdot \mathbf{r}}{4\pi\epsilon_0 r^3} = \lim_{r \rightarrow \infty} [\phi(P_e) - \psi(P_e)]. \quad (6)$$

This yields

$$\mathbf{P} = \epsilon_0(\kappa - 1) \iint_S \phi(p) \tilde{n}_p dS_p. \quad (7)$$

For our configuration the dipole moment will be in a direction opposite to that of the initial field. Its magnitude is shown in fig. 5, where a comparison of the computed dipole moment of a dielectric cube and those of two significant spheres, the inscribed sphere and the equivolume sphere, is evidenced.

Fig. 6 shows a comparison of the dipole moments per unit volume of a sphere and of a cube, and gives an indication of the effectiveness of these two shapes in producing dipole moment.

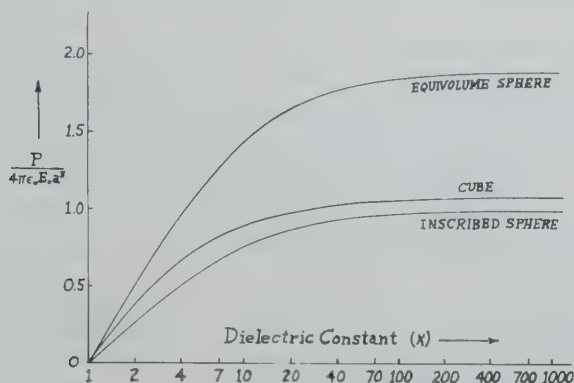


Fig. 5. Dipole moments of dielectric bodies.

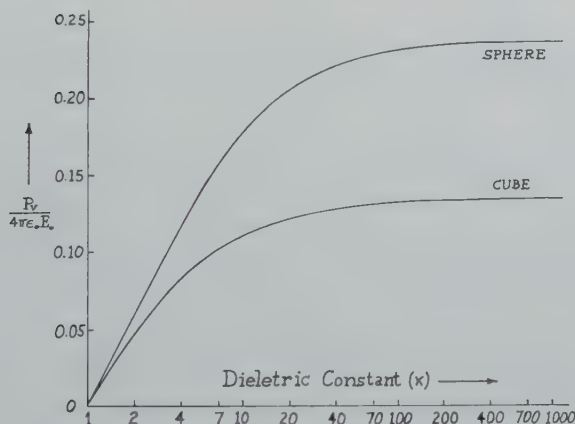


Fig. 6. Dipole moments (per unit volume) of dielectric bodies.

Acknowledgement. The authors wish to express their appreciation to the Wisconsin Alumni Research Foundation for its financial support of this project and to the University of Wisconsin Numerical Analysis Laboratory for granting use of its IBM 650 computer.

Received 27th December, 1960.

REFERENCES

- 1) Phillips, H. B., J. Math. Phys. **13** (1934) 261.
- 2) Edwards, T. W., Perturbation of a Uniform Electrostatic Field by a Dielectric Cube, University of Wisconsin, Department of Electrical Engineering, M.S. Thesis, 1960.

SKEW RAY TRACING THROUGH TORIC REFRACTING SURFACES

by J. BECKER

N.V. Optische Industrie De Oude Delft, Delft, the Netherlands

Summary

A simplified method for skew ray tracing through toric refracting surfaces is described and formulae are given.

§ 1. *Introduction.* In an optical system having only concentric refracting and reflecting spherical surfaces all aberrations due to lack of symmetry are absent. A system of only three components may constitute a wide angle objective of reasonably large aperture ¹⁾. The image plane is spherical too, and for an infinite object it is concentric with the surfaces of the optical system. Used as a camera objective, the film should adapt to this spherical focal plane. With sufficient accuracy this is only possible for a relatively small field of view. However, the image surface can be made cylindrical by introducing a field-flattening lens. In that case the accurate positioning of the film presents no difficulties. When flattening the image plane for a vertical section (fig. 1), the field of view in the horizontal plane still has no limitations, whereas now the useful vertical field of view is limited by the unsharpness, which is due to the aberrations introduced by refraction through the field-flattening lens. This lens has a toric surface and a cylindrical surface on which we want the image to be formed. A method for ray-tracing through toric refracting surfaces has been described by Murray ²⁾. As will be shown, a simplified calculation scheme may also be used.

§ 2. *Determination of the point of intersection.* We first determine the point of intersection Q of a ray, coming from a point P on the

preceding surface of the system, with the toric surface. At the top T (fig. 1) the toric refracting surface has radii of curvature r and r_c . The distance between the centres of curvature $a \equiv r_c - r$.

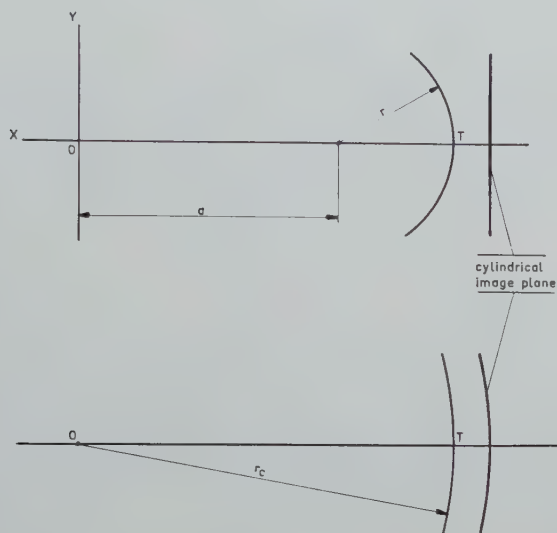


Fig. 1. Cross-section of the toric refracting system.

The system of coordinates has been taken such that the origin O coincides with the centre of curvature with the radius r_c . The x -axis coincides with the optical axis, the y -axis is the axis of the cylindrical image surface. The toric surface is given by the equation

$$f(x, y, z) = (x^2 + y^2 + z^2 + a^2 - r^2)^2 - 4a^2(x^2 + z^2) = 0. \quad (1)$$

For the incident ray through the point P (ξ, η, ζ) , with cosines L, M, N relative to the x -, y - and z -axis respectively, the equation reads

$$x = \xi - L\rho, \quad y = \eta - M\rho, \quad z = \zeta - N\rho, \quad (2)$$

where ρ is the distance between the point P and the point Q (x, y, z) .

We find after substituting (2) in (1) and some rearrangements that

$$\rho^4 - 4b\rho^3 + 2\rho^2(2b + c^2 - 2a^2d) + 4\rho(2a^2e - bc) + c^2 - 4a^2g = 0, \quad (3)$$

in which

$$\begin{aligned} b &= \xi L + \eta M + \zeta N, \\ c &= \xi^2 + \eta^2 + \zeta^2 + a^2 - r^2, \\ d &= L^2 + N^2, \\ e &= \xi L + \zeta N, \\ g &= \xi^2 + \zeta^2. \end{aligned} \quad (4)$$

Now ρ is the skew distance between the two refractive surfaces. For the principal ray of the pencil to which PQ belongs, the distance may be calculated from a conventional meridional ray tracing. Supposing this distance to be t , we find, putting $\rho = t + \Delta$

$$(t + \Delta)^4 - 4b(t + \Delta)^3 + 2(t + \Delta)^2(2b^2 + c - 2a^2d) + 4(t + \Delta)(2a^2e - bc) + c^2 - 4a^2g = 0. \quad (5)$$

If Δ is small, Δ^4 and Δ^3 may be neglected, while Δ can be found from the resulting quadratic equation, giving a first approximation for ρ . The value of ρ thus found is corrected in one or two steps by insertion into (3), until ρ has the accuracy required. The coordinates of the point of intersection Q of the ray and the toric surface are then given by (2).

§ 3. *The refraction.* The cosines of the angles with the co-ordinate axes for the normal in Q (x, y, z) on the toric surface are given by

$$\frac{1}{w} \frac{\partial f}{\partial x}, \quad \frac{1}{w} \frac{\partial f}{\partial y}, \quad \frac{1}{w} \frac{\partial f}{\partial z}, \quad (6)$$

in which

$$w^2 = \left(\frac{\partial f}{\partial x} \right)^2 + \left(\frac{\partial f}{\partial y} \right)^2 + \left(\frac{\partial f}{\partial z} \right)^2.$$

The angle of incidence φ between the ray and the normal in Q is found from

$$\cos \varphi = \frac{1}{w} \left(\frac{\partial f}{\partial x} L + \frac{\partial f}{\partial y} M + \frac{\partial f}{\partial z} N \right). \quad (7)$$

The angle of refraction φ' is obtained by application of Snell's law. Hence, the value of $C = n' \cos \varphi' - n \cos \varphi$ is determinable. This value is needed for the calculation of the direction of the refracted ray.

The cosines L' , M' and N' for the refracted ray in the coordinate system of fig. 1 may be determined as follows (fig. 2). Take a length of line $QA = n$ on the incident ray, a length of line $QB = n'$ on the refracted ray. Then AB is parallel to the normal (fig. 2). If

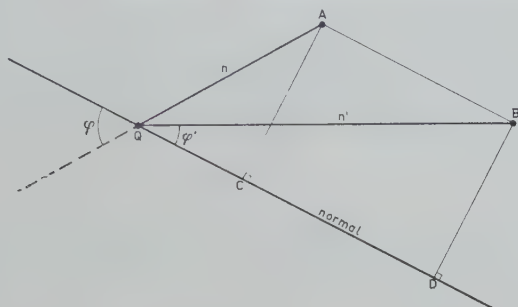


Fig. 2. Determination of the cosines for the ray, refracted at the toric surface.

the broken line $QA-AB-BQ$ is projected on to the coordinate axes, the sum of the projections on the x -, y - and z -axis is in each case equal to zero. The cosines and lengths of the three parts of the broken line are given in table I.

TABLE I

	cosines			lengths
QA	L	M	N	n
AB	$\frac{1}{w} \frac{\partial f}{\partial x}$	$\frac{1}{w} \frac{\partial f}{\partial y}$	$\frac{1}{w} \frac{\partial f}{\partial z}$	$n' \cos \varphi' - n \cos \varphi = C$
BQ	L'	M'	N'	n'

When projecting on to the x -axis we find

$$nL + C \frac{1}{w} \frac{\partial f}{\partial x} - n'L' = 0$$

or

$$L' = \frac{n}{n'} L + \frac{C}{n'} \frac{1}{w} \frac{\partial f}{\partial x}. \quad (8)$$

Projection on to y - and z -axis respectively gives

$$M' = \frac{n}{n'} M + \frac{C}{n'} \frac{1}{w} \frac{\partial f}{\partial y}, \quad (9)$$

$$N' = \frac{n}{n'} N + \frac{C}{n'} \frac{1}{w} \frac{\partial f}{\partial z}. \quad (10)$$

§ 4. *Conclusion.* In this way the refracted ray is completely determined, and its intersection with the image plane can be found. In practice with a desk computer the ray tracing of seven rays from one pencil was achieved in three hours, making it fairly easy to obtain the best correction. The formulae are also suited for programming the calculating scheme for an electronic digital computer. As a direct application the design of a new(horizon)-camera ³⁾ having a horizontal field of 360° and a cylindrical image plane may be mentioned.

Acknowledgement. Thanks are due to Prof. Dr. A. Bouwers for his interest in this work and for the permission to publish it.

Received 10th January, 1961.

REFERENCES

- 1) Bouwers, A., *Achievements in Optics*, ed. Elsevier, Amsterdam 1946.
- 2) Murray, A. E., *J. Opt. Soc. Amer.* **44** (1954) 9.
- 3) Bouwers, A., *Photogrammetria* no. 4, 1956.

ON THEOREMS OF MINIMUM ENERGY DISSIPATION IN MAGNETOHYDRODYNAMICS

by L. N. TAO

Department of Mechanics, Illinois Institute of Technology, Chicago, Illinois, U.S.A.

Summary

This paper is concerned with some theorems on the dissipation of energy in magnetohydrodynamics. It is shown that when certain conditions, (2.21) or (2.27) of the text, are satisfied, the steady motion of an electrically conducting incompressible fluid has an absolute minimum of energy dissipation. Furthermore, when the same conditions are satisfied, an unsteady motion with steady boundary conditions always tends to its steady state, which is stable as well as unique. The present theorems are also applicable to ordinary hydrodynamics and magnetohydrostatics. A brief implication of these theorems is discussed.

§ 1. *Introduction.* In studies of magnetohydrodynamics many authors have considered the situation of equipartition of kinetic and magnetic energy. The suggestion is based on the physical argument that fluid motion tends to stretch the magnetic lines of force, and so to increase the magnetic energy. The magnetic energy, however, cannot be increased indefinitely. When the magnetic energy becomes too large, the tension along the lines of force checks any further extension of them. Thus in an ultimate steady state the inertial forces can be expected to be comparable with the effects of tension along the lines of forces. In other words, an equipartition between kinetic and magnetic energies or its approximate form will finally be reached in a steady state. This was first suggested by Walén¹⁾. Elsasser²⁾ also commented that the equipartition may be conjectured from the symmetric form of the governing equations of magnetohydrodynamics. In the following we intend to give some theorems which may be helpful in discussions on equipartition of energy.

In ordinary hydrodynamics, i.e., in the absence of magnetic fields, some general theorems on minimum energy dissipation have been discussed by Helmholtz ³⁾, Korteweg ⁴⁾ and Rayleigh ⁵⁾. They are generalized in this communication to magnetohydrodynamics. In the first part it will be shown that under certain conditions, which include equipartition of energy as a special case, the total energy dissipation of a motion within a closed system is a minimum when compared to any other motion subject to identical boundary conditions. Hence a motion with equipartition of energy possesses an absolute minimum of energy dissipation. Furthermore, we will also show that when the velocity and magnetic fields are maintained steady over the boundary, an unsteady motion satisfying previous conditions always tends to its steady state. The type of steady motion finally attained is stable, as well as unique. The motion with equipartition of energy is one of these motions, and therefore it is a stable equilibrium.

§ 2. *Steady motion.* Consider a steady motion M of an incompressible fluid in a region D bounded by a closed surface Σ . Let its velocities be u_i and magnetic field intensities H_i . Then the total dissipation of energy of the motion ^{*)} is

$$Q = \int_D (\phi_m + \phi_e) dv = \int_D (T_{ij}u_{i,j} + j^2/\sigma) dv, \quad (2.1)$$

where ϕ_m and ϕ_e are, respectively, the mechanical (viscous) and electromagnetic dissipation per unit volume. T_{ij} is the viscous stress tensor, j_i the current density ^{**)} and σ the electric conductivity.

Now let us consider another motion M^* characterized by velocity u_i^* and magnetic field intensity H_i^* which satisfy the same boundary conditions as the motion M . Writing $u_i^* = u_i + u_i'$ and $H_i^* = H_i + H_i'$, we then have u_i' and H_i' vanishing at all points on the boundary. The dissipation of this alternative motion M^* is

^{*)} The summation convention is used in this paper.

^{**)} Within the validity of magnetohydrodynamic approximation, i.e. negligible displacement current, the current density may be interpreted with reference to either a moving or stationary observer.

$$\begin{aligned}
Q^* &= \int_D (\phi_m^* + \phi_e^*) dv = \\
&= \int_D (T_{ij} + T'_{ij})(u_{i,j} + u'_{i,j}) dv + \int_D \frac{1}{\sigma} (j_i + j'_i)(j_i + j'_i) dv = \\
&= \int_D (\phi_m + \phi_m') dv + \int_D (T'_{ij}u_{i,j} + T_{ij}u'_{i,j}) dv + \\
&+ \int_D (\phi_e + \phi_e') dv + 2 \int_D \frac{1}{\sigma} j_i j'_i dv. \tag{2.2}
\end{aligned}$$

From the viscous stress tensor

$$T_{ij} = \eta(u_{i,j} + u_{j,i}), \tag{2.3}$$

where η is the viscosity of the fluid, we find

$$\begin{aligned}
T_{ij}u'_{i,j} &= \eta(u_{i,j} + u_{j,i})u'_{i,j} = \\
&= \eta(u'_{i,j} + u'_{j,i})u_{i,j} = T'_{ij}u_{i,j}. \tag{2.4}
\end{aligned}$$

The substitution of (2.4) into (2.2) gives

$$Q^* = Q + Q' + 2 \int_D T_{ij}u'_{i,j} dv + 2 \int_D \frac{1}{\sigma} j_i j'_i dv. \tag{2.5}$$

Now we intend to show that these two integrals vanish under certain conditions. Using integration by parts, the first integral of the right hand side of (2.5) is

$$\int_D T_{ij}u'_{i,j} dv = T_{ij}u'_{i,j}|_{\partial D} - \int_D u'_i T_{ij,j} dv = - \int_D \eta u'_i u_{i,jj} dv, \tag{2.6}$$

since the u'_i vanish on the boundary and $u_{i,i} = 0$.

From the momentum equation of an electrically conducting liquid in the steady state

$$\rho u_j u_{i,j} = \rho F_i + L_i - \dot{p}_{,i} + \eta u_{i,jj}, \tag{2.7}$$

where ρ is the density, F_i the extraneous force, $L_i = \mu \varepsilon_{ijk} j_j H_k$ the Lorentz force and μ the magnetic permeability, we may write

$$\int_D T_{ij}u'_{i,j} dv = \int_D u'_i [\rho u_j u_{i,j} - \mu H_j H_{i,j} - \rho F_i + \dot{p}_{,i} + \mu (H_j H_j)_{,i}] dv. \tag{2.8}$$

Now, we observe that if ρF_i has a potential Ω ,

$$\rho F_i = -\Omega_{,i} \quad (2.9)$$

and

$$u_j u_{i,j} - \frac{\mu}{\rho} H_j H_{i,j} = \psi_{,i}/\rho, \quad (2.10)$$

where ψ is a single-valued function in the domain, then the integral

$$\int_D T_{ij} u'_{i,j} dv = 0 \quad (2.11)$$

by virtue of

$$\int_D u'_i (\omega + \psi)_{,i} dv = u'_i (\omega + \psi)|_{\partial D} - \int_D (\omega + \psi) u'_{i,i} dv = 0, \quad (2.12)$$

$$\omega = p + \mu H_j H_j + \Omega, \quad (2.13)$$

due to $u'_i = 0$ on the boundary and $u'_{i,i} = 0$.

Using the vorticity vector ξ_i and Maxwell's equation between j_i and H_i and taking the curl of (2.10), we then have the condition

$$\nabla^2 (\xi \times \mathbf{u}) = \nabla^2 \left(\frac{\mu}{\rho} \mathbf{j} \times \mathbf{H} \right) \quad (2.14)$$

in place of (2.10).

The second integral in (2.5) may be written as

$$\int_D \frac{1}{\sigma} j_i j'_i dv = \int_D \frac{1}{\sigma} H'_{i,j} (H_{i,j} - H_{j,i}) dv = - \int_D \frac{1}{\sigma} H'_i H_{i,jj} dv. \quad (2.15)$$

Here we have used integration by parts and Maxwell's equation $H_{j,j} = 0$. The elimination of the electric field intensities E_i from Maxwell's equations (steady case) and Ohm's law

$$\begin{aligned} \varepsilon_{ijk} E_{k,j} &= 0, \\ \varepsilon_{ijk} H_{k,j} &= j_i, \\ j_i &= \sigma (E_i + \mu \varepsilon_{ijk} u_j H_k) \end{aligned} \quad (2.16)$$

gives ²⁾

$$u_j H_{i,j} - \frac{1}{\sigma \mu} H_{i,jj} - H_j u_{i,j} = 0. \quad (2.17)$$

Therefore, if

$$u_j H_{i,j} - H_j u_{i,j} = \chi_{,i}, \quad (2.18)$$

where χ is another single-valued function in the domain, then (2.15) is

$$\int_D \frac{1}{\sigma} j_i j_i' dv = \int_D \mu H_i' (u_j H_{i,j} - H_j u_{i,j}) dv = \int_D \mu H_i' \chi_{,i} dv = 0. \quad (2.19)$$

We may also replace (2.18) by taking the curl of (2.18); this gives

$$\nabla^2(\mathbf{u} \times \mathbf{H}) = 0. \quad (2.20)$$

Hence when

$$\begin{aligned} \rho \mathbf{F} &= -\nabla \Omega, \\ \nabla^2(\boldsymbol{\xi} \times \mathbf{u}) &= \nabla^2 \left(\frac{\mu}{\rho} \mathbf{j} \times \mathbf{H} \right), \\ \nabla^2(\mathbf{u} \times \mathbf{H}) &= 0, \end{aligned} \quad (2.21)$$

(2.5) is simply

$$Q^* = Q + Q'. \quad (2.22)$$

Furthermore, Q' is non-negative. It vanishes only when $u'_{i,j} = 0$ and $H'_{i,j} = 0$. This implies that u_i' and H_i' remain constant throughout the domain as if the system moved as a rigid body in a "frozen" magnetic field. Since we have u_i' and H_i' vanishing on the boundary, no such motion is possible. Therefore, the motion \mathbf{M} which satisfies conditions (2.21) is unique and possesses an absolute minimum of dissipation of energy. In conclusion, we have

Theorem IA. In magnetohydrodynamics (without displacement current) the motion of an electrically conducting viscous incompressible fluid has a smaller dissipation of energy than any other motion which obeys the same boundary conditions, provided conditions (2.21) are satisfied.

In the case of equipartition of energy ⁶⁾, i.e.

$$\mathbf{u} = \sqrt{\frac{\mu}{\rho}} \mathbf{H}, \quad (2.23)$$

the motion clearly satisfies (2.21), and hence its energy dissipation is an absolute minimum.

In theorem IA we have used the fact that the extraneous force $\rho \mathbf{F}_i$ has a potential Ω . This condition may be removed. In that case from (2.6) we have

$$\int_D T_{ij} u'_{i,j} dv = - \int_D \eta u_i' u_{i,jj} dv, \quad (2.24)$$

The integral vanishes when

$$u_{i,jj} = 0 \quad (2.25)$$

or

$$\nabla^2 \xi = 0. \quad (2.26)$$

This condition is satisfied by Stokes' flow or any other "slow" motion, i.e., motion void of inertial force effect.

Writing the equivalence of $\nabla^2(\mathbf{u} \times \mathbf{H}) = 0$ in the form of $\nabla^2 \mathbf{j} = 0$, we have

Theorem IB. In the case of the non-existence of a potential Ω of the extraneous force, theorem IA is true, provided the motion satisfies

$$\nabla^2 \xi = 0, \quad \nabla^2 \mathbf{j} = 0. \quad (2.27)$$

§ 3. *Unsteady motion.* Consider an unsteady motion of an electrically conducting liquid in a region D bounded by a surface Σ . The boundary conditions of the motion are maintained steady. Let its velocity and magnetic field intensity be u_i and H_i . Then the time rate of change of dissipation of energy is

$$\frac{\partial Q}{\partial t} = \frac{\partial}{\partial t} \int_D (T_{ij} u_{i,j} + j^2/\sigma) dv. \quad (3.1)$$

We interchange the differentiation and integration and obtain

$$\frac{\partial Q}{\partial t} = \int_D \left(T_{ij} u_{i,jt} + T_{ij,t} u_{i,j} + \frac{2}{\sigma} j i j_{i,t} \right) dv. \quad (3.2)$$

Replacing primes by $(\)_{,t}$ in (2.4), we find

$$T_{ij,t} u_{i,j} = T_{ij} u_{i,jt}. \quad (3.3)$$

Equation (3.2) then becomes

$$\frac{\partial Q}{\partial t} = 2 \int_D (T_{ij} u_{i,jt} + j i j_{i,t}/\sigma) dv. \quad (3.4)$$

Similar to the verification of (2.6) and (2.15), we find

$$\frac{\partial Q}{\partial t} = -2 \int_D (\eta u_{i,t} u_{i,jj} + H_{i,t} H_{i,jj}/\sigma) dv \quad (3.5)$$

since $u_{i,t} = 0$ and $H_{i,t} = 0$ on the boundary.

Using the governing equations of magnetohydrodynamics ²⁾

$$\begin{aligned} \rho u_{i,t} + \rho u_j u_{i,j} &= \rho F_i + L_i - p_{,i} + \eta u_{i,jj}, \\ H_{i,t} + u_j H_{i,j} - \frac{1}{\sigma \mu} H_{i,jj} - H_j u_{i,j} &= 0 \end{aligned} \quad (3.6)$$

and (2.21), we have

$$\frac{\partial Q}{\partial t} = -2 \int_D \left(\rho u_{i,t} u_{i,t} + \frac{1}{\sigma} H_{i,t} H_{i,t} \right) dv. \quad (3.7)$$

The integral is non-negative, implying that the dissipation diminishes continuously until $\partial Q / \partial t = 0$. $\partial Q / \partial t$ vanishes only when $u_{i,t} = 0$ and $H_{i,t} = 0$, i.e. when a steady state is reached. Hence when the boundary conditions remain steady on Σ , the motion in D tends to its steady state if the motion satisfies (2.21).

Furthermore, the ultimate state, the steady motion, is unique. Suppose an unsteady motion to lead to two different ultimate motions $M^{(1)}$ and $M^{(2)}$. The existence of conditions (2.21) assures the linearity of the governing equations. It means that the difference of these two motions is also a possible motion with $u_i = 0$ and $H_i = 0$ on the boundary. But such a motion necessarily comes to rest. The motions $M^{(1)}$ and $M^{(2)}$ must tend to become and to remain identical. If one of these two motions is steady, the other must finally come to coincide with it. This assures the uniqueness. Hence, the steady motion with equipartition of energy is a stable one. In conclusion, we have

Theorem IIA. In magnetohydrodynamics an unsteady motion of an electrically conducting viscous incompressible fluid with boundary conditions being maintained steady will always tend to its steady state, which is stable and unique, provided conditions (2.21) are satisfied.

In the absence of a potential Ω of the extraneous force we can similarly prove the following theorem:

Theorem IIB. In the case of the non-existence of a potential Ω of the extraneous force, theorem IIA is true, provided the motion satisfies conditions (2.27).

§ 4. *Discussions.* In the previous sections we have shown that a motion of an electrically conducting incompressible fluid satisfying (2.21) or (2.27) has an absolute minimum of energy dissipation.

The result is applicable to ordinary hydrodynamics by letting the magnetic field be zero. It reduces to the theorems discussed by Helmholtz, Korteweg and Rayleigh. The theorems may also be used in magnetohydrostatics. In the study of hydrostatic equilibrium of magnetic stars, Chandrashekhar and his associates in a series of papers ^{7) 8)} have discussed the stability of a force-free field, which means that $(\text{curl } \mathbf{H}) \times \mathbf{H}$ vanishes. Clearly, the force-free field satisfies (2.21); it possesses a minimum dissipation of energy.

By the inspection of the governing equations of magnetohydrodynamics, it is seen that when (2.21) or (2.27) hold, the equations are linear ones. Superposition is therefore applicable. A discussion by Kapur ⁹⁾ on the possibilities of superposition of solutions has led to (2.21) in somewhat less general form.

When (2.21) or (2.27) hold, a minimum principle is involved. This readily suggests that the variational method may be used in some magnetohydrodynamic and magnetohydrostatic problems.

Acknowledgment. This investigation was sponsored by the Office of Naval Research under contract Nonr 1406(06) with Illinois Institute of Technology.

Received 3rd January, 1961.

REFERENCES

- 1) Walén, C., Ark. Mat. Astr. Fys. **33a** (1946) 18.
- 2) Elsasser, W. M., Phys. Rev. **79** (1950) 183.
- 3) Helmholtz, H. von, Verh. Naturhist.-med. Vereins, 1868; Wiss. Abh. i, p. 223.
- 4) Korteweg, D. J., Phil. Mag. (5) xvi (1883) 112.
- 5) Lord Rayleigh, Phil. Mag. (6) xxvi (1913) 776; Papers vi, p. 187.
- 6) Cowling, T. G., Magnetohydrodynamics, Interscience Publishers, Inc., 1957.
- 7) Chandrashekhar, S., Proc. Nat. Acad. Sci. **42** (1956) 1, 273; **43** (1957) 24; **44** (1958) 285, 842; Astrophys. J. **124** (1956) 232.
- 8) Woltjer, L., Proc. Nat. Acad. Sci. **44** (1958) 489, 833.
- 9) Kapur, J. N., Appl. Sci. Res. **A8** (1960) 198.

MARTINUS NIJHOFF — PUBLISHER — THE HAGUE

MICROPROJECTION WITH X-RAYS

by

ONG SING POEN

TECHNOLOGICAL UNIVERSITY, DELFT

One of the 5 types of X-ray microscopes is the projection microscope, originally proposed by Von Ardenne in 1939 and realized by Cosslett and Nixon in 1951.

With the aid of an ultra-fine-focus X-ray tube with a spot diameter of 1–0.1 micron, an enlarged X-ray shadow image is projected on a screen or film. Due to negligible scattering and refraction clear absorption images can be obtained. A special feature is the great depth of focus. Thus ideal stereo images can be made, showing the three dimensional mass absorption distribution of the specimen. This will be of great importance for both research (medical, biological, metallurgical, criminological, etc.) and technology (rubber-, textile-, paper-industry etc.). In "Microprojecton with X-rays" the author describes his experiences in constructing and applying the projection microscope in practice, covering five years of research in this field. His book will serve as a guide to those who are intending to explore the possibilities of this type of microscope.

1959. 132 pages on art paper. With 42 figures and 38 illustrations.

Guilders 12.50

Obtainable through any bookseller or from the publisher